JGR Earth Surface

RESEARCH ARTICLE
10.1029/2020JF005571

Influence of Dunes on Channel-Scale Flow and Sediment Transport in a Sand Bed Braided River

Christopher A. Unsworth[1,2], Andrew P. Nicholas[1], Philip J. Ashworth[3], James L. Best[4], Stuart N. Lane[5], Daniel R. Parsons[6], Gregory H. Sambrook Smith[7], Christopher J. Simpson[3], and Robert J. P. Strick[3]

[1]Geography, College of Life and Environmental Science, University of Exeter, Exeter, UK, [2]Now at National Oceanography Centre, Joseph Proudman Building, Liverpool, UK, [3]Division of Geography and Geology, School of Environment and Technology, University of Brighton, Brighton, UK, [4]Departments of Geology, Geography and GIS, Mechanical Science and Engineering and Ven Te Chow Hydrosystems Laboratory, University of Illinois at Urbana-Champaign, Urbana, IL, USA, [5]Institute of Earth Surface Dynamics, Faculté des Géosciences et de l'Environnement, Université de Lausanne, Lausanne, Switzerland, [6]Institute of Energy and Environment, Faculty of Science, University of Hull, Hull, UK, [7]School of Geography, Earth, Environmental Sciences, University of Birmingham, Birmingham, UK

Key Points:
- 3-D CFD is used to quantify the flow structure over dunes superimposed upon large-scale alternate bars in a natural river
- Net influence of dunes is to enhance lateral flows and reduce velocities over bar tops by as much as 30%
- Dunes can amplify or dampen the deflection of sediment down lateral bar slopes

Supporting Information:
- Supporting Information S1

Correspondence to:
C. A. Unsworth,
chrisaunsworth@outlook.com

Citation:
Unsworth, C. A., Nicholas, A. P., Ashworth, P. J., Best, J. L., Lane, S. N., Parsons, D. R., et al. (2020). Influence of dunes on channel-scale flow and sediment transport in a sand bed braided river. *Journal of Geophysical Research: Earth Surface*, *125*, e2020JF005571. https://doi.org/10.1029/2020JF005571

Received 16 FEB 2020
Accepted 5 OCT 2020
Accepted article online 13 OCT 2020

Abstract Current understanding of the role that dunes play in controlling bar and channel-scale processes and river morphodynamics is incomplete. We present results from a combined numerical modeling and field monitoring study that isolates the impact of dunes on depth-averaged and near-bed flow structure, with implications for morphodynamic modeling. Numerical simulations were conducted using the three-dimensional computational fluid dynamics code OpenFOAM to quantify the time-averaged flow structure within a 400 m × 100 m channel using digital elevation models (DEMs) for which (i) dunes and bars were present within the model and (ii) only bar-scale topographic features were resolved (dunes were removed). Comparison of these two simulations shows that dunes enhance lateral flows and reduce velocities over bar tops by as much as 30%. Dunes influence the direction of modeled sediment transport at spatial scales larger than individual bedforms due to their effect on topographic steering of the near-bed flow structure. We show that dunes can amplify, dampen, or even reverse the deflection of sediment down lateral bar slopes, and this is closely associated with 3-D and obliquely orientated dunes. Sediment transport patterns calculated using theory implemented in depth-averaged morphodynamic models suggest that gravitational deflection of sediment is still controlled by bar-scale topography, even in the presence of dunes. However, improved parameterizations of flow and sediment transport in depth-averaged morphodynamic models are needed that account for the effects of both dune- and bar-scale morphology on near-bed flow and sediment transport.

1. Introduction

Over the past three decades, significant advances have been made in numerical modeling of river processes and evolution using both two-dimensional "2-D" depth-averaged (Baar et al., 2019; Bridge, 1993; Chavarrías et al., 2019; Iwasaki et al., 2016; Lane & Richards, 1998; Langendoen et al., 2016; Nelson, 1990; Nicholas et al., 2013; Osada et al., 2020; Schuurman et al., 2013; Sloff & Mosselman, 2012) and three-dimensional "3-D" vertically resolved approaches (Bradbrook et al., 2000; Doré et al., 2016; Giri & Shimizu, 2006; Lane et al., 1999; Nabi et al., 2013; Wu et al., 2000; Yamaguchi et al., 2019; Zgheib & Balachandar, 2019). This body of work has shown that such models are capable of simulating the morphodynamics of a wide range of channel types, including meandering, braided, and anabranching rivers (Baar et al., 2019; Nicholas, 2013; Schuurman et al., 2013, 2016; Schuurman & Kleinhans, 2015; Sun et al., 2015).

The relative simplicity and computational efficiency of 2-D models compared to 3-D approaches (those based on the 3-D Reynolds-averaged Navier-Stokes [RANS] equations or eddy-resolving models) means that simulation of decadal to centennial river evolution over large (10^2–10^5 m) spatial scales is currently more practical using 2-D models (e.g., Baar et al., 2019; Nicholas, 2013) than 3-D. However, compared to 3-D models, such 2-D approaches inevitably involve a higher degree of abstraction of the governing physics (Lane et al., 1999; Sloff & Mosselman, 2012). For example, 2-D depth-averaged models must parameterize, rather than represent explicitly, phenomena such as secondary circulation, the effects of topographic

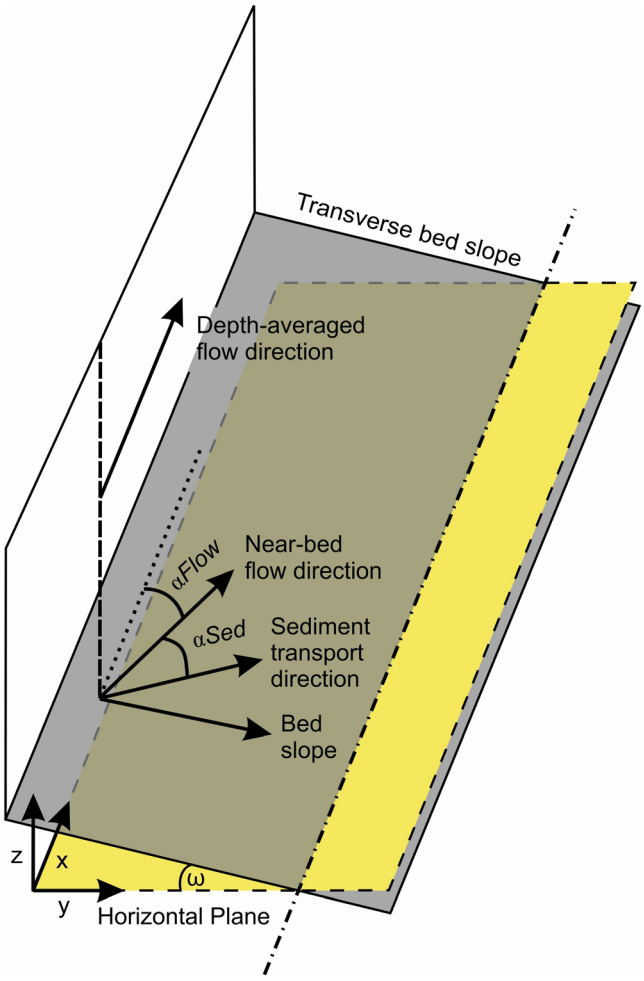

Figure 1. Definition of the coordinate system and processes under investigation herein for the hypothetical case of depth-averaged flow aligned parallel to the *x* direction (downstream) and perpendicular to a transverse bed slope. Directions *x*, *y*, and *z*, correspond to velocities *u*, *v*, and *w*. *αFlow* is the deviation between the depth-averaged flow and the near-bed flow direction. *αSed* is the deviation between the near-bed flow and the bed sediment transport direction, resulting from gravitational deflection of sediment in the direction of the transverse bed slope ($\tan\omega\partial z/\partial y$). Adapted from Sekine and Parker (1992).

features (e.g., dunes and ripples), and sediment transport processes (e.g., Furbish et al., 2012; Schmeeckle, 2014) that cannot be resolved by the model mesh. Consequently, depth-averaged models necessarily adopt a highly simplified treatment of many factors that control the linkages between the flow, sediment transport, and channel change within natural rivers.

These issues can be illustrated by considering the relationships between flow and sediment transport directions as represented within a typical 2-D morphodynamic model, for the simple case of a river with a transverse bed slope perpendicular to the depth-averaged fluid flow direction (Figure 1). When calculating sediment transport directions, 2-D depth-averaged models typically account for at least two processes that promote a deviation between the mean flow and sediment transport directions: first, the deviation between the depth-averaged and near-bed flow direction (labeled *αFlow* in Figure 1) resulting from secondary circulation of the flow (Kleinhans et al., 2008; Struiksma et al., 1985); and second, the deviation between the near-bed flow and sediment transport directions (labeled *αSed* in Figure 1), which results from the deflection of sediment particles down the transverse slope of the river bed due to the effects of gravity (Antoniazza et al., 2019; Apsley & Stansby, 2008; Baar et al., 2019; Engelund, 1974; Francalanci & Solari, 2008; Ikeda, 1982; Sekine & Parker, 1992; Struiksma et al., 1985).

It has been demonstrated that river morphology and dynamics simulated using 2-D models can be highly sensitive to the parameterization of the processes outlined above (Antoniazza et al., 2019; Baar et al., 2019; Mosselman & Binh Le, 2016; Nicholas et al., 2013; Schuurman et al., 2013; Sloff & Mosselman, 2012). In addition, while existing parameterizations of transverse slope effects on sediment transport have been developed and evaluated using laboratory data sets (Baar et al., 2018; Koch & Flokstra, 1981; Sieben & Talmon, 2011), their applicability at field scales remains uncertain. This is due, in part, to the greater complexity of field environments, which are characterized by multiple scales of topography (e.g., channels, bars, and bedforms) that influence flow and sediment transport. For example, dunes and ripples are ubiquitous in sand bed rivers and exert a significant control on hydraulic roughness and hence on the channel-scale spatial distribution of flow (Karim, 1995; Lefebvre et al., 2016; Rodrigues et al., 2015; Sandbach et al., 2012, 2018). Flow structures and turbulence produced by dunes are also commonly 3-D (Baar et al., 2018; Best, 2005; Lefebvre, 2019; Maddux, McLean, et al., 2003; Maddux, Nelson, et al., 2003; Omidyeganeh & Piomelli, 2013a, 2013b) and have been proposed to break down, or suppress, secondary flow structures usually found in meander bends and braided rivers (Abad et al., 2013; Best, 2005; Blanckaert, 2010; Dietrich et al., 1979; Drake et al., 1988; Konsoer et al., 2016; Parsons et al., 2007). Moreover, dunes give rise to complex patterns of local bed slope that may have a significant influence on the gravitational deflection of sediment (Baar et al., 2018; Sieben & Talmon, 2011; Weij, 2012). How these processes interact with, and modify, patterns of flow and sediment transport at the scale of whole channels and bars has yet to be quantified.

The extent to which existing parameterizations of flow and sediment transport processes in depth-averaged morphodynamic models (e.g., as shown in Figure 1) require revision to account for the effects discussed above remains largely unknown. Furthermore, evaluating and improving these parameterizations in field settings is problematic due to the difficulty of obtaining contemporaneous flow, topography, and sediment transport data sets of sufficient resolution and quality. The work presented herein aims to address these

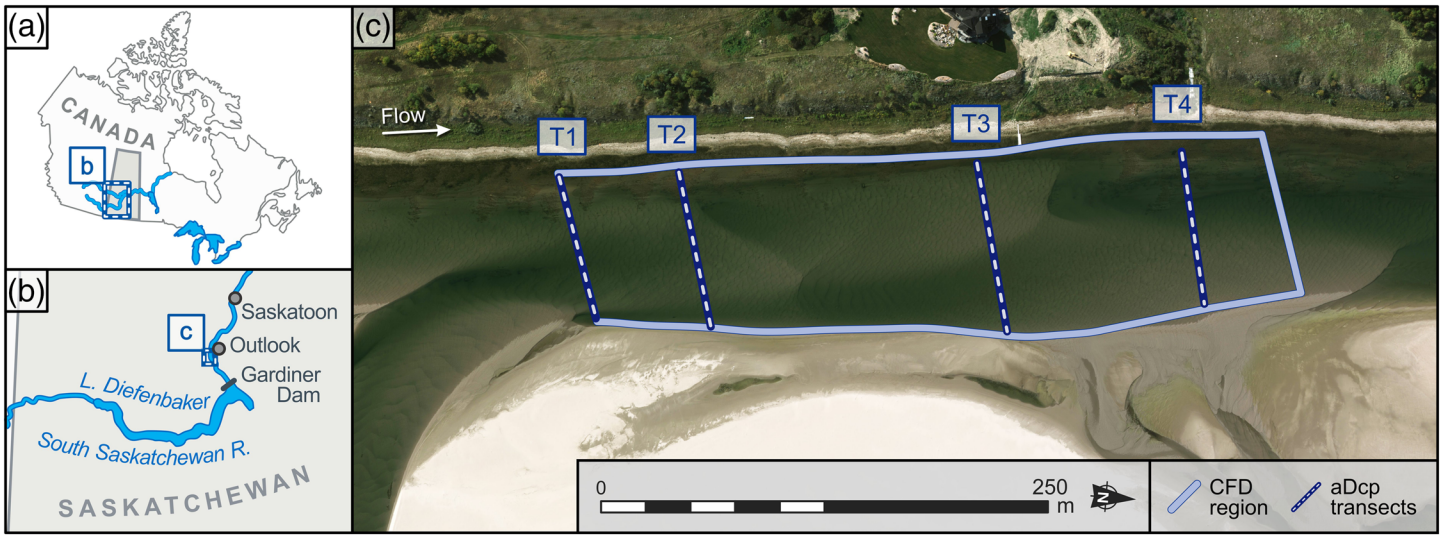

Figure 2. Location of the South Saskatchewan River in Canada (a), near the town of Outlook, Saskatchewan, Canada (b). (c) The study reach and location of the flow measurement transects (dashed lines labeled T1 to T4). Image taken on 2 September 2016; at time of measurement the flow discharge in the channel shown in (c) was 40 $m^3\ s^{-1}$. See Strick et al. (2019) for aerial photography of the braidplain morphology of the South Saskatchewan River.

issues by (i) applying 3-D computational fluid dynamics (CFD) to quantify the effect of dunes on bar-scale flow characteristics within a sand bed river, and (ii) evaluating the implications for the parameterization of sand transport on transverse bed slopes within depth-averaged morphodynamic models.

2. Methods

2.1. Study Area

Field measurements and numerical modeling were conducted within a 400 m long reach of the South Saskatchewan River, near the town of Outlook (51°30′N, 107°03′W), Canada (Figure 2). The South Saskatchewan River is a braided sand bed channel with a mean bed material grain size of approximately 0.3 mm and a mean gradient of approximately 0.23 m km^{-1} (Cant, 1976; Parker et al., 2013; Sambrook Smith et al., 2006). The discharge that inundates the largest nonvegetated sand braid bars is 280 $m^3 s^{-1}$ (Cant & Walker, 1978; Lunt et al., 2013; Sambrook Smith et al., 2010), and the bankfull discharge (above which islands and the floodplain are inundated) is approximately 1,240 $m^3 s^{-1}$. The study reach is located approximately 15 km downstream of the Gardiner Dam (51°16′12″N, 106°52′15″W), which was completed in 1967 and traps >98% of suspended sediment in Lake Diefenbaker (Wiebe & Drennan, 1973). This sediment trapping promotes relatively clear water within the study reach, even at high flow stages, which is fundamental to the acquisition of the bathymetric data described below.

2.2. Field Data Collection

A survey was undertaken in September 2016 to measure the flow and morphology of the study reach (see Figure 2c). The reach was selected to include a straight channel with well-defined bar pool topography and simple inlet and outlet conditions and to be small enough to facilitate 3-D CFD modeling at a high (~0.08 m) spatial resolution. Average water depth in the study reach was 0.8 m, discharge at the time of measurement was 40 $m^3\ s^{-1}$ (River discharge was ~80 $m^3\ s^{-1}$), and the reach average depth mean velocities were ~0.5 m s^{-1}. A digital elevation model (DEM) for the reach was constructed from specially commissioned aerial imagery (pixel resolution 0.06 m) captured at a height of ~1,500 m from a fixed-wing airplane with an UltraCamXp sensor. Full details of the procedures used in DEM construction and associated error analysis are outlined in Strick et al. (2019). In brief, a 0.06 m (horizontal) resolution DEM was constructed using a combination of large format Structure-from-Motion (SfM) photogrammetry (using the commercial software Pix4D) and a regression model between water depth and image brightness (after Lane et al., 2010). SfM techniques were applied principally in emergent areas and within a

20–40 m wide section along the true left bank where the channel bed is composed predominantly of gravel. This generated a DEM in these areas with a horizontal spatial resolution of 0.24 m. A depth-brightness model was applied to the inundated areas of the reach, where the channel is sand bedded, to produce a DEM with a horizontal resolution of 0.06 m. This depth-brightness regression model was developed and validated for the aerial imagery using water depth measurements obtained with a Navisound© NS 215 system with a Reson© TC 2024 200 kHz high-resolution dual frequency single-beam echo sounder (SBES) operating at a sampling frequency of 10 Hz, with simultaneous geographical location provided by a Leica© 1,230 Real-Time Kinematic (RTK) dGPS system. The DEMs generated using SfM and the depth-brightness model were merged along the left bank of the study reach to produce a single DEM for use in CFD mesh generation. Dune geometry was measured on this DEM via zero-crossing analysis. Average dune lengths were approximately 2.5 m with a maximum of 6 m, and average dune heights were approximately 0.17 m with a maximum of 0.30 m.

Repeat flow surveys of the channel were undertaken along cross-channel transects to provide CFD model boundary conditions and data for model evaluation. A minimum of four repeat surveys (pairs in opposite directions) were conducted to measure the mean flow structure (Szupiany et al., 2007), with T1 having six repeats. Three-dimensional flow velocities were recorded using a Sontek© M9© acoustic Doppler current profiler (aDcp) mounted onto a small zodiac boat. The position of the aDcp was also recorded using the RTK dGPS. Velocities are calculated relative to the instrument head and corrected using the dGPS-calculated boat speed and heading. The error in aDcp measurements is recorded by the instrument as the difference in measured vertical velocity from pairs of beams (Mueller & Wagner, 2009; Muste et al., 2004). The mean instantaneous error velocity for these surveys was −0.074 m s^{-1}, and the aDcp manufacturer reports an accuracy of ±0.05 m s^{-1} for velocity measurements. The aDcp data were collected in pulse coherent mode, averaging seven pings per second, and were averaged to 1 Hz to improve the signal-to-noise ratio. Three-dimensional flow velocities were measured on individual track lines and gridded to a resolution of 0.1 m (vertical bin size) and 0.25 m (horizontal bin size) using the VMT aDcp postprocessing software (Parsons et al., 2013).

2.3. CFD Modeling

The open source CFD package OpenFOAM (Weller et al., 1998) was applied to solve the RANS equations for incompressible flow (Equations 1 and 2). This procedure splits the flow variables into time-averaged (e.g., $\overline{U}$) and fluctuating (e.g., U') components:

$$\frac{\partial \overline{\boldsymbol{U}}_i}{\partial \boldsymbol{X}_i} = 0, \tag{1}$$

$$\frac{\partial \overline{\boldsymbol{U}}_i}{\partial t} + \overline{u}_j \frac{\partial \overline{\boldsymbol{U}}_i}{\partial \boldsymbol{X}_j} = \frac{1}{\rho}\frac{\partial p}{\partial \boldsymbol{X}_i} + \frac{1}{\rho}\frac{\partial}{\partial \boldsymbol{X}_i}\left(\mu \frac{\partial \overline{\boldsymbol{U}}_i}{\partial \boldsymbol{X}_i} - \rho \overline{\boldsymbol{U}_i' \boldsymbol{U}_j'}\right), \tag{2}$$

where p is pressure, ρ is water density, and the dynamic viscosity is μ.

The terms in Equation 2 are expressed as time-averaged quantities, with the Reynolds Stress terms originating from the product of the fluctuating components. These terms are modeled by a Boussinesq approximation (written in Tensor form):

$$-\overline{\boldsymbol{U}_i' \boldsymbol{U}_j'} = \nu_t \left(\frac{\partial \overline{\boldsymbol{U}}_i}{\partial \boldsymbol{X}_j} + \frac{\partial \overline{\boldsymbol{U}}_j}{\partial \boldsymbol{X}_i}\right) - \frac{2}{3} k \delta_{ij}, \tag{3}$$

where $\boldsymbol{U}$ is the 3-D velocity vector $\boldsymbol{U} = [u\ v\ w]$, $\boldsymbol{X}$ is the Cartesian coordinate vector $\boldsymbol{X} = [x\ y\ z]$, δ_{ij} is the Kronecker delta ($\delta_{ij} = 1$ if $i = j$, otherwise $\delta_{ij} = 0$), and k is the turbulent kinetic energy. The eddy viscosity (ν_t) in Equation 3 was modeled using the Re-Normalization Group theory (RNG) k-ε turbulence closure (Yakhot & Orszag, 1986) that has been shown to perform well in riverine applications, where high strain and flow separation are common (e.g., Bradbrook et al., 2000; Hardy et al., 2011; Marjoribanks et al., 2017; Sandbach et al., 2012). Herein, the turbulent viscosity $\nu_t (= C_\mu k^2/\varepsilon)$ is computed from the turbulent kinetic energy (k) and turbulent dissipation rate (ε). These are obtained by solving their own scalar transport equations:

$$\frac{\partial(k\boldsymbol{U}_i)}{\partial \boldsymbol{X}_i} = \frac{\partial}{\partial \boldsymbol{X}_i}\left[\frac{v_t}{\sigma_k}\frac{\partial k}{\partial \boldsymbol{X}_j}\right] - P_k - \varepsilon, \tag{4}$$

$$\frac{\partial(\varepsilon\boldsymbol{U}_i)}{\partial \boldsymbol{X}_i} = \frac{\partial}{\partial \boldsymbol{X}_i}\left[\frac{v_t}{\sigma_k}\frac{\partial k}{\partial \boldsymbol{X}_j}\right] + \frac{\varepsilon}{k}(C_{1\varepsilon}P_k - C_{2\varepsilon}\varepsilon), \tag{5}$$

where

$$P_k = -\overline{\boldsymbol{U}_i'\boldsymbol{U}_j'}\left(\frac{\partial \overline{\boldsymbol{U}}_j}{\partial \boldsymbol{X}_i} + \frac{\partial \overline{\boldsymbol{U}}_i}{\partial \boldsymbol{X}_j}\right), \tag{6}$$

is the production of turbulent kinetic energy through shear, $C_\mu = 0.0845$, $\sigma_k = \sigma_\varepsilon = 0.7194$, $C_{1\varepsilon} = 1.42$, and

$$C_{2\varepsilon} = 1.68 + C_\mu \eta^3 \frac{1 - \eta/4.38}{1 + 0.012\eta^3}, \tag{7}$$

are constants which have been determined experimentally, and $\eta\left(= k\sqrt{P_k/v_t}/\varepsilon\right)$ is a dimensionless parameter (Yakhot & Orszag, 1986). A uniform near-bed cell thickness of 0.0035 m with an equivalent sand grain roughness (k_s) of 0.0017 m was implemented herein to ensure appropriate dimensionless wall distance (z^+) values in the near-bed grid cell. z^+ is defined as

$$z^+ = \frac{zu^*}{v}, \tag{8}$$

where z is the vertical coordinate, v is the kinematic viscosity, and u^* is the friction velocity computed assuming an equilibrium boundary condition (law of the wall). For the near bed, $k\ \left(= u^*2/\sqrt{C_\mu}\right)$ and dissipation $\varepsilon\ \left(= C_\mu^{3/4}k^{3/2}/\kappa\Delta z\right)$, where κ is the von Karmon constant (0.41) and Δz is the distance between the bed and the center of the near bed cell. The specific wall functions used in OpenFOAM were "*epsilonWallFunction*" for ε, "*kqRWallFunction*" for k, and "*nutkRoughWallFunction*" for v_t, with a no-slip condition on velocity and zero-normal gradient for pressure. Mean z^+ values for both simulations were 55, with medians of 58 for the DEM without dunes and 57 for the DEM with dunes (described below), well above the minimum value of $z^+ = 30$ and below $z^+ = 300$, which are the bounds of the wall roughness model (i.e., inside the log law layer). In the present modeling, the wall roughness function represents the net effect of both grain roughness and small bedforms (e.g., ripples) that cannot be resolved by the CFD mesh (see below).

The OpenFOAM solver "*simpleFOAM*" (a steady-state solver for incompressible, turbulent flow) was used to compute the pressure using the Semi-Implicit Method for Pressure-Linked Equations "SIMPLE" (Patankar & Spalding, 1972) algorithm. The free surface was represented in the model with a rigid-lid approximation (e.g., Stoesser et al., 2008; Xie et al., 2013), adopted herein as the water surface was flat with a Froude number ~0.15. Inlet conditions were defined using the aDcp surveys at the same channel discharge (40 $m^3\ s^{-1}$) at T1 (Figure 2). The depth-averaged velocity entering the domain at each point across the inlet section was determined from the aDcp data and used to run a 1-D vertical boundary layer profile at each point across the inlet channel to generate profiles of horizontal velocity, turbulent kinetic energy (k), and the dissipation rate (ε) for each boundary grid cell, while maintaining the unit discharge across the inlet equal to that of the aDcp data. Vertical velocity components at the inlet to the model domain were set to 0. A Neumann pressure condition was set at the outlet, with a uniform pressure of 0. The outlet was located 5 m downstream from the zone used to interpret model results.

To provide the minimum acceptable numerical dissipation for the mesh, second-order central differencing numerical schemes were used for gradients and second-order bounded central differencing for divergence, and an unbounded second-order deferred corrected scheme was employed for the Laplacian surface normal gradients (see Jasak, 1996; & Robertson et al., 2015 for details and sensitivity tests of the OpenFOAM numerics). Convergence criteria were tested iteratively and set to a tolerance of 1×10^{-8} for pressure and 1×10^{-10} for velocity, k and ε. Solver tolerances were set to 1×10^{-10} for pressure and 1×10^{-12} for

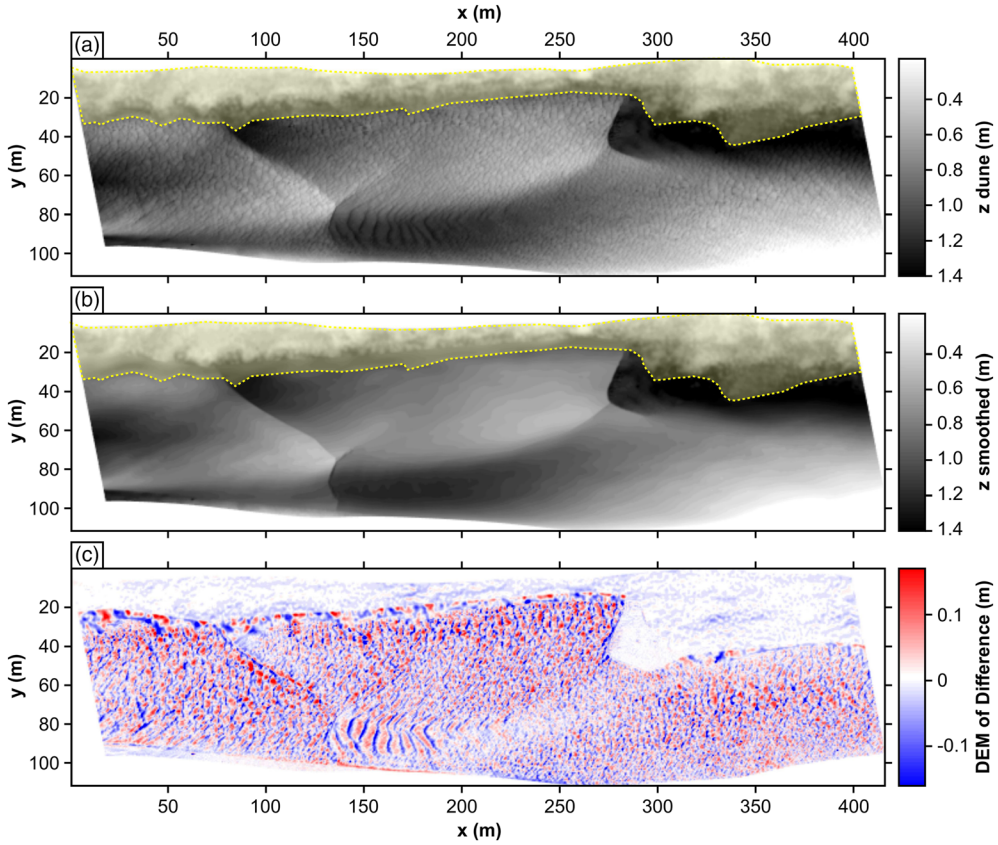

Figure 3. Bed topography for DEMs used in the 3-D CFD simulations (elevations are measured relative to the water surface). (a) *Dune DEM*. (b) *Smoothed DEM* after the removal of the dunes. (c) Elevation difference between the two DEMs. The area inside the yellow dashes in (a) and (b) is mixed sand, gravel, and cobbles. Discharge at the time of survey was ~40 $m^3\ s^{-1}$.

velocity. Flow variables were recorded at 128 regularly spaced locations within the computational domain at each computational time step. Using this sampling, the convergence of the simulation was tested and confirmed by a consistent lack of variation in the values of flow variables. Convergence for both simulations carried out herein occurred before the preset criteria with pressure converging first, above the solver tolerance.

2.4. CFD Mesh Generation

To investigate the effect of dunes on the 3-D flow field, and the associated implications for the parameterization of sediment transport in 2-D morphodynamic models, CFD simulations were conducted using two meshes, one with the measured channel morphology and one with the dune-scale topography removed from the DEM. To remove dunes from the original 0.06 m resolution DEM without affecting the representation of bank or bar topography, the outlines of the banks and bar fronts were identified visually in ARCMAP©, and raster masks produced to separate each bar surface for individual filtering. River banks and the lee slopes of the unit bars were therefore not modified. To remove the dunes from the individual bar tops, a moving-average, weighted-mean filter was used, with a window size of 6 m × 1 m, with the longest axis in the downstream direction. Figure 3 shows the resulting bed topographies, referred to hereafter as the *Dune DEM* and *Smoothed DEM*. Following this process, the two surface meshes were compared quantitatively to confirm that the larger bar-scale morphology of the reach had not been altered by the removal of dune-scale topography (the mean and maximum differences between the two DEMs for topography at 10 m resolution were 0.08 and 1.4 mm). Therefore, the differences in mean flow structure reported below are only due to the removal of dunes, as opposed to changes in the larger-scale channel morphology.

Both DEMs were down-sampled to a resolution of 0.24 m and then used to construct 0.08 m horizontal resolution CFD surface DEMs using 2-D bilinear interpolation. This procedure produced two 0.08 m resolution DEMs, which were each adjusted to limit CFD mesh gradients, cell skewness, and nonorthogonality. This was achieved by applying a gradient filter, which altered bed elevations over approximately 4% of each model domain by approximately 3 mm. Finally, two structured finite volume CFD meshes were constructed for CFD modeling, both comprising 4,948 × 1,172 × 20 cells in the downstream, cross-stream, and vertical directions, respectively. Horizontal mesh resolution was an average of 0.08 m with 20 cells in the vertical and a planar water surface. Cells in the vertical become finer toward the bed as a power law function of depth to ensure that the majority of the vertical grid cells were close to the bed in areas of greater velocity gradient. The vertical resolution of the boundary-fitted mesh therefore varied as a function of flow depth and height above the bed. The average vertical grid cell size is 0.04 m, with a standard deviation of 0.03 m. Grid independence tests were carried out by performing three simulations using grids with horizontal resolutions of 0.03, 0.08, and 0.12 m. Comparison of global and local flow characteristics for these simulations (see details in supporting information) demonstrated model results were relatively insensitive to grid resolution. All results generated for the study reach that are presented herein were generated using 0.08 m resolution meshes. Additional model validation was performed via comparison with the laboratory data of Maddux, McLean, et al. (2003) and Maddux, Nelson, et al. (2003), and is reported in the supporting information.

2.5. Method of Analyzing Model Results

To assess the role that dunes might play in bed sediment transport within a depth-averaged morphodynamic models framework, quantification of the effect of dunes on flow at larger scales (i.e., than a single dune), are needed. Five metrics describing the relationships between the depth-averaged flow, near-bed flow, and sediment transport directions (as illustrated in Figure 1 and discussed in section 1) were calculated. Throughout the manuscript there are three symbols used to define particular variables: θ = a direction (in degrees); δ = the difference between a variable compared between simulations, and α = the difference between variables in a single simulation.

The effect of dunes on the mean flow was evaluated by calculating $\delta Mean$, defined as the deviation between the depth-averaged flow directions in the simulations using the *Dune DEM* and the *Smoothed DEM*:

$$\delta Mean = \theta DAF_{dune} - \theta DAF_{smoothed} \tag{9}$$

where $\theta\ DAF_{dune}$ and $\theta\ DAF_{smoothed}$ are the depth-averaged angular planform flow directions for the simulations that used the *Dune DEM* and the *Smoothed DEM*, respectively, such that positive values indicate flow rotated toward the left bank in the *Dune DEM* simulation relative to the *Smoothed DEM* simulation. Similarly, the deviation between the near-bed flow directions in the two simulations (δBed) was calculated as

$$\delta Bed = \theta NBF_{dune} - \theta NBF_{smoothed} \tag{10}$$

where $\theta\ NBF_{dune}$ and $\theta\ NBF_{smoothed}$ are the near-bed angular planform flow directions for the simulations that use the *Dune DEM* and *Smoothed DEM*, respectively.

To investigate the influence of dunes on bed sediment transport, in the context of depth-averaged morphodynamic model parameterizations of these processes, near-bed flow velocities derived from the model simulations were used to calculate sediment transport directions. In order to relate the results of this analysis to past work on transverse slope effects on sediment transport (e.g., Baar et al., 2018; Sekine & Parker, 1992), sediment transport directions were quantified using an approach adopted in the Delft3D morphodynamic model:

$$\theta Sed = \tan(S_2/S_1) \tag{11a}$$

$$S_1 = S_1^{'} - S_2^{'}.Fn \tag{11b}$$

$$S_2 = S_2{}' - S_1{}'.Fn \tag{11c}$$

$$Fn = \beta \sqrt{\frac{\tau_c \partial z}{\tau \partial n}} \tag{11d}$$

where θ *Sed* is the angular planform sediment transport direction, S_1 and S_2 are the sediment transport direction in the x and y directions (respectively) *after* accounting for gravitational deflection of sediment by transverse slope effects, and S_1' and S_2' are the sediment transport direction in the x and y directions (respectively) *before* correcting for transverse slope effects. τ and τ_c are the bed shear stress and critical bed shear stress, respectively, $\partial z/\partial n$ is the bed slope normal to the near-bed flow direction, and β is an empirical constant. The unit sediment transport components prior to adjusting for transverse slope effects are specified by assuming that sediment transport moves in the direction of the near-bed flow, which obviates the need to determine the magnitude of the sediment transport rate. Although the parameter β is a function of many factors including grain size and bed roughness (see Baar et al., 2018), our aim in this first instance is to estimate an upper bound for the magnitude of transverse slope effects; therefore, calculations are based on the case where sediment transport is at the threshold of motion and assume $\beta = 1.5$ (the default value in Delft3D). The implications of this choice of value are discussed further below. It should also be noted that although sediment transport directions derived using Equations 11a–11d lead to deflection of sediment in the local downslope direction, these equations do not include an explicit representation of avalanching processes in the leeside of dunes, because the complexity of such processes precludes a simple treatment of their net effect on sediment transport (Drake et al., 1988; Nield et al., 2017; Pelletier et al., 2015; Sutton et al., 2013).

The deviation (δSed) between the sediment transport directions calculated using Equations 11a–11d, for the model simulations using the *Dune DEM* and the *Smoothed DEM*, was calculated as

$$\delta Sed = \theta Sed_{dune} - \theta Sed_{smoothed} \tag{12}$$

where θSed_{dune} and $\theta Sed_{smoothed}$ are the sediment transport directions derived for the *Dune DEM* simulation and the *Smoothed DEM* simulation, respectively. The difference (δ *Flow*) between the near-bed flow direction (θNBF) and the depth-averaged flow direction (θDAF) in the model results generated using the *Dune DEM* and *Smoothed DEM* was calculated as

$$\delta Flow = (\theta NBF_{dune} - \theta DAF_{dune}) - (\theta NBF_{smoothed} - \theta DAF_{smoothed}) \tag{13}$$

This metric quantifies the degree to which the deviation between the near-bed and depth-averaged flow directions changes in the presence of dunes. An equivalent metric (δTop) was derived to quantify the extent to which dunes influence the deviation between the near-bed flow direction and the sediment transport direction (i.e., including the effects of sediment deflection due to the transverse bed slope):

$$\delta Top = (\theta Sed_{dune} - \theta NBF_{dune}) - (\theta Sed_{smoothed} - \theta NBF_{smoothed}) \tag{14}$$

Depth-averaged models are typically implemented at spatial resolutions that are coarser than individual dunes. Additionally, such models must parameterize the effects of the processes that are driven by dune-scale topography, rather than represent these processes explicitly. It is therefore relevant to consider whether differences in flow (and sediment transport) that are evident in the two model simulations at fine spatial resolution are also evident at coarser spatial scales that are more typical of those used in depth-averaged morphodynamic models. To evaluate this, the CFD model results, and associated metrics defined by Equations 9–14, are examined below at two spatial scales: (i) at the resolution of the 3-D CFD modeling (referred to hereafter as the *fine-resolution* results), and (ii) following spatial averaging of model results at a horizontal resolution of 5 m (referred to hereafter as the *spatially averaged* results). The spatial resolution of 5 m was selected to be large enough to ensure that most grid cells include at least one dune, while also being small enough to resolve the bar-scale morphology within the model domain. This is also a resolution at which it would be appropriate to apply a 2-D depth-averaged morphodynamic model within the study reach.

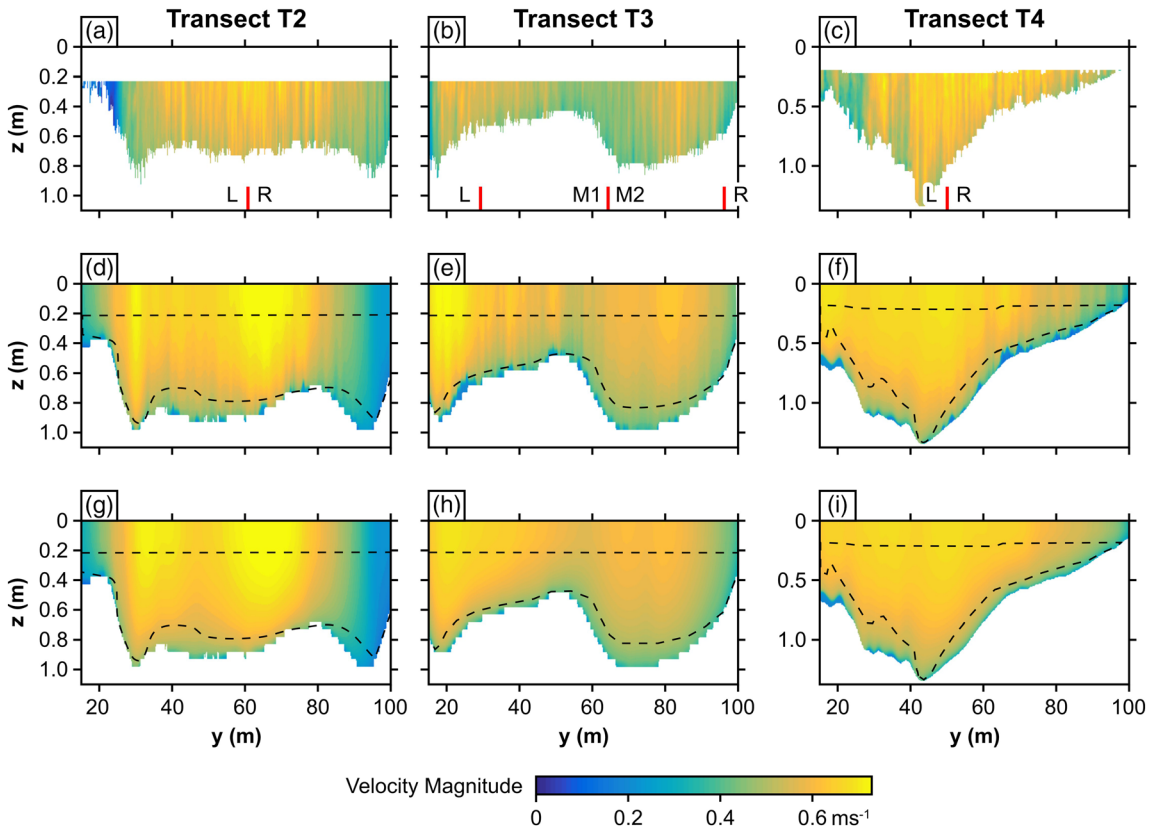

Figure 4. Contoured images of the velocity magnitudes at aDcp Transect Locations T2 (left column), T3 (middle column), and T4 (right column). Sections are oriented looking downstream. The top row displays the aDcp measurements; the middle row displays the *Dune DEM* simulation results; and the bottom rows show the *Smoothed DEM* simulation results. The aDcp instrument has a blanking distance of 0.2 m and does not collect near-bed or near-surface velocities, which are prone to error. Dashed lines in Panels (d) to (i) indicate the boundary of the aDcp data. Subsections of each transect that displayed consistent trends were also individually regressed, and the demarcations of these subsections is shown at the bottom of Panels (a)–(c). Associated scatter plots and tables of statistics for these subsection regressions are given in the supporting information (Table S3 and Figure S4). Flow is through the page (in the *x* direction).

3. Results

3.1. Model Comparison With Measured Velocities

Figures 4 and 5 compare modeled flow velocity magnitudes and horizontal directions with velocities surveyed using the aDcp at Transects T2 to T4 (i.e., downstream of the model inlet at T1, see Figure 2). The agreement between modeled and observed velocity directions (Figure 5 and Table S3) is good in most locations. For example, both models replicate the transition from diverging flow in upstream areas (e.g., at Transect T2) to flow that is predominantly from right to left in downstream areas (e.g., at Transect T4).

Previous studies have demonstrated that perfect replication of observed velocities is unlikely at cm scales due to multiple factors, including flow measurement errors (such as inherent instrument error and geolocation error), unresolved turbulence structures, differences between the CFD mesh and natural topography, and the computational constraints on obtaining true grid independence (Marjoribanks et al., 2017; Sandbach et al., 2012). Consequently, the purpose of the comparison conducted herein is to (i) assess if the model replicates the measured average flow structure; (ii) confirm that differences between measured and modeled velocities do not invalidate the model as a quantitative description of the flow (Lane & Richards, 2001; Lane et al., 2005; French, 2010); and (iii) ascertain whether the inclusion of dunes within the model mesh produces flow fields that provide an improved fit to the field data. A statistical analysis is detailed in the supporting information summaries the overall qualitative (Figures 4 and 5) and quantitative (Table S3) comparisons between the model results and aDcp data sets. The analysis indicates that both models reproduce the macroscale structure of the flow, but the inclusion of dunes into the model DEM results in improved reproduction of the observed flow field. One important aspect of the difference in flow fields using the

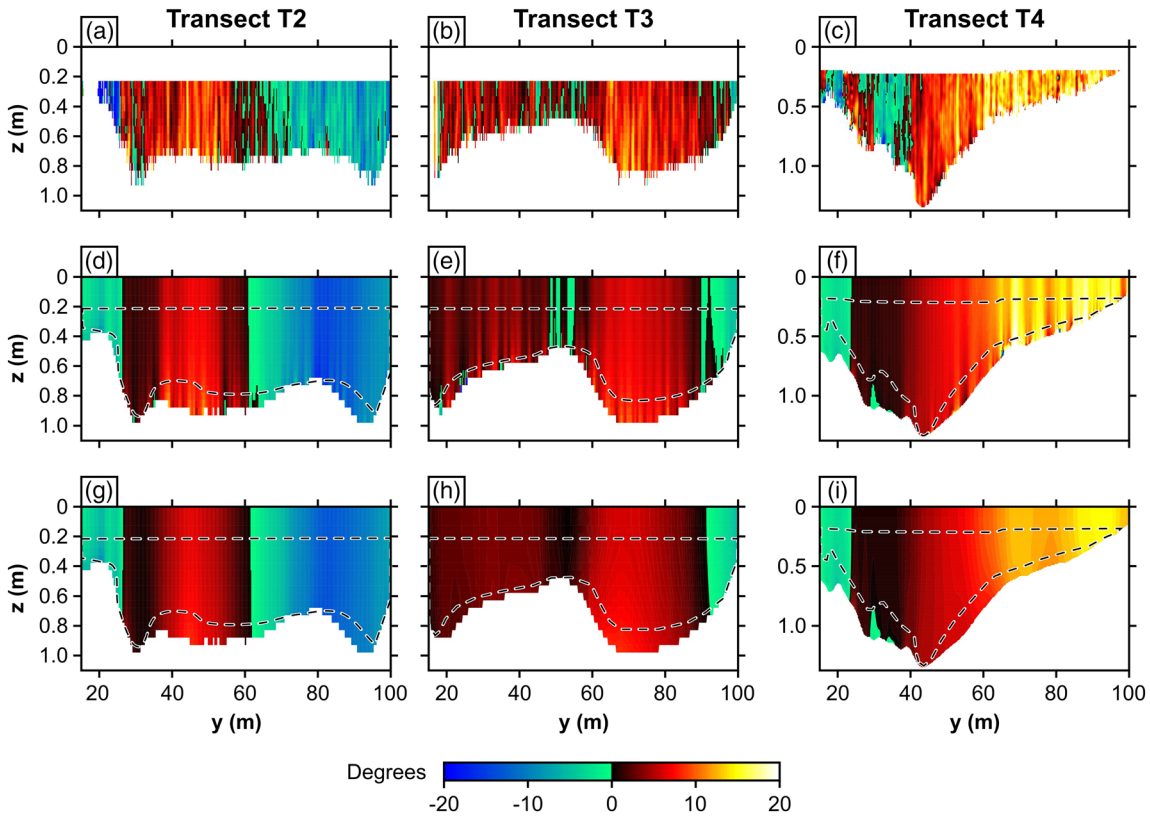

Figure 5. Contoured images of the velocity direction at aDcp Transect Locations T2 (left column), T3 (middle column), and T4 (right column). Sections are oriented looking downstream. Flow is into the page at 0°, positive values (red-yellow) are toward the left bank, and negative values (green-blue) are toward the right bank. (a–c) The aDcp measurements; (d–f) the *Dune DEM* simulation results; and (g–i) the *Smoothed DEM* simulation results. The aDcp instrument has a blanking distance of 0.2 m and does not collect near-bed or near-surface velocities, which are prone to error. Dashed lines in Panels (d) to (i) indicate the boundary of the aDcp data.

Dune DEM is the increased cross-channel variability in the velocity direction and magnitudes compared to the *Smoothed DEM* simulations. This horizontal banding has been seen in many aDcp transects and has been attributed to field measurements capturing large-scale turbulence from form-roughness, and/or a lack of repeat measurements to produce satisfactory averages (Engel & Rhoads, 2016; Parsons et al., 2005; Szupiany et al., 2012). Yet herein, the *Dune DEM* simulation does replicate this effect, suggesting that it is not just an artifact of field sampling but is also an inherent aspect of the effect of dunes on the time-averaged 3-D flow structure.

3.2. Effect of Dunes on Near-Bed Flow Structure

While Figures 4 and 5 illustrate that the model results generated using the two DEMs exhibit similar macro-scale patterns of velocity magnitude and direction, differences between the results of the two simulations are greatest in the near-bed regions due to the influence of bedforms. Figure 6 shows an example of near-bed morphology and flow vector patterns over a 5 m × 6 m patch of bed located immediately upstream of a bar front. Dune leesides on the top of this bar tend to be orientated oblique to the dominant downstream flow direction, such that near-bed flow directions are rotated significantly relative to the *Smoothed DEM* case. Consequently, near-bed flow velocities exhibit significant variations in local magnitude and direction in the presence of dunes (Figure 6a) that are almost entirely absent in the model results generated using the *Smoothed DEM* (Figure 6b). Such flow structures in the leesides of oblique, or 3-D dunes, have been well documented for individual dunes (Allen, 1968; Omidyeganeh & Piomelli, 2013a, 2013b; Sieben & Talmon, 2011; Talmon et al., 1995; Walker, 1999; Walker & Shugar, 2013) but until now have proven difficult to measure or simulate across multiple bedforms.

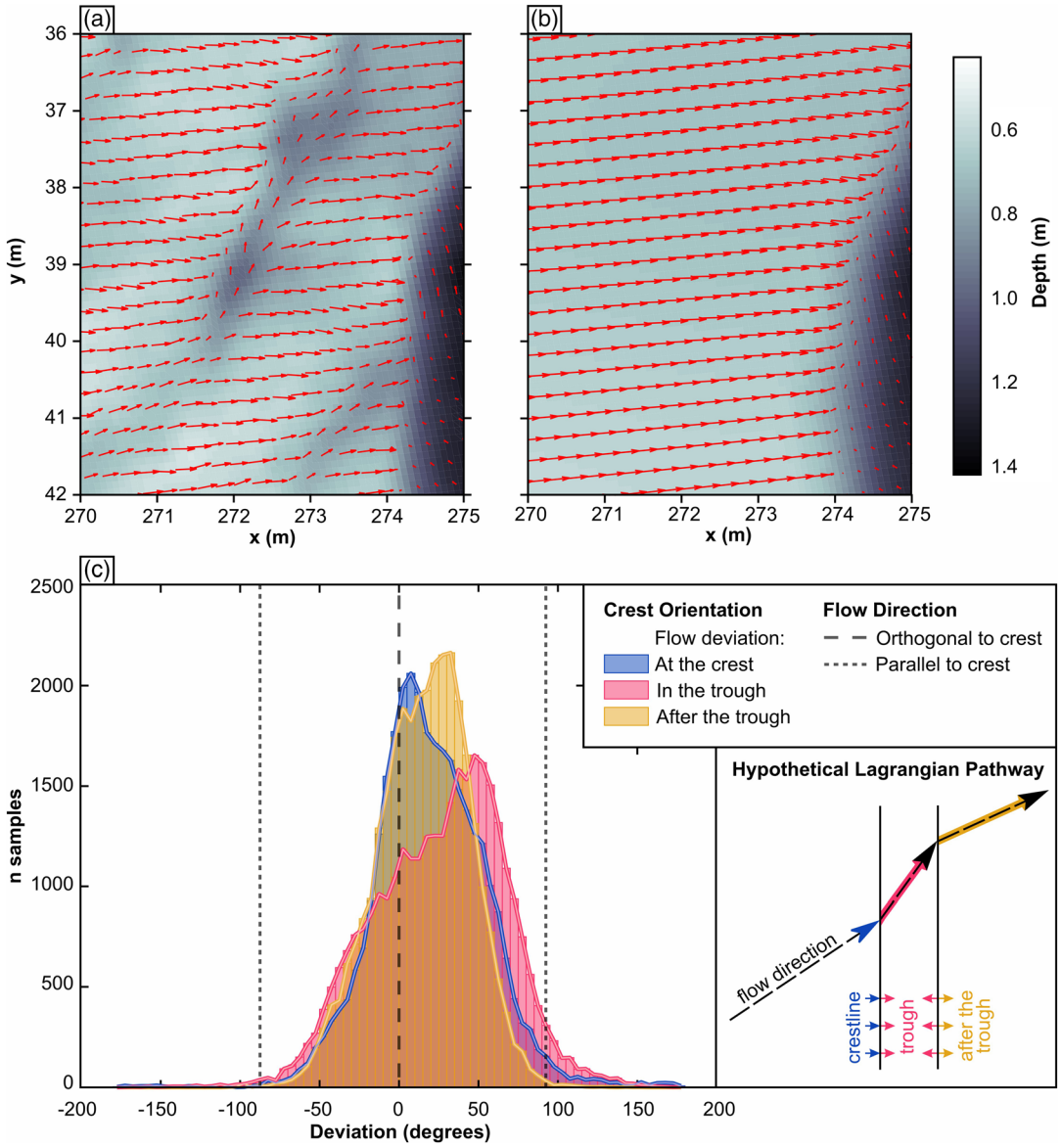

Figure 6. Near-bed flow vectors over a 5 m × 6 m patch of bed taken from (a) the *Dune DEM* simulation and (b) the *Smoothed DEM* simulation. For clarity, every fourth vector is plotted. (c) Histogram of near-bed flow directions, expressed as deviations relative to the direction perpendicular to the local dune crestline orientation. Histograms are plotted for flow at the crest (blue), within the downstream dune trough (pink), and downstream of the trough (yellow). The schematic diagram to the right illustrates these three regions for the hypothetical Lagrangian pathway followed by a fluid parcel flowing over a 2-D dune with a crestline that is oblique to the flow.

To assess the changes in flow direction over the dunes in the study reach, individual dune crests and their orientations were digitized by hand (Figure 7a), and the corresponding near-bed flow direction downstream of the crest was measured over a distance of 1 m (see supporting information for method). These measurements were made for dunes across the whole study reach (Figure 6c) and show that only ~12% of dune crestlines are orientated orthogonal to the flow direction just upstream of the dune crest (±5°), whereas ~67% of crests are oblique to the flow (between ±5° and ±50°) and ~20% are highly oblique to the flow (± > 50°). In the dune troughs, the distribution of flow directions is heavily skewed, with a peak in the distribution at ~50°, indicating that near-bed flow in the dune troughs has been deflected toward the orientation of the dune crests but that flow parallel to the crestline orientation is uncommon. Downstream of the troughs (the yellow histogram), the frequency distribution of flow directions peaks between the crest and trough distributions, indicating flow realignment toward the flow directions found at the dune crests. This pattern is

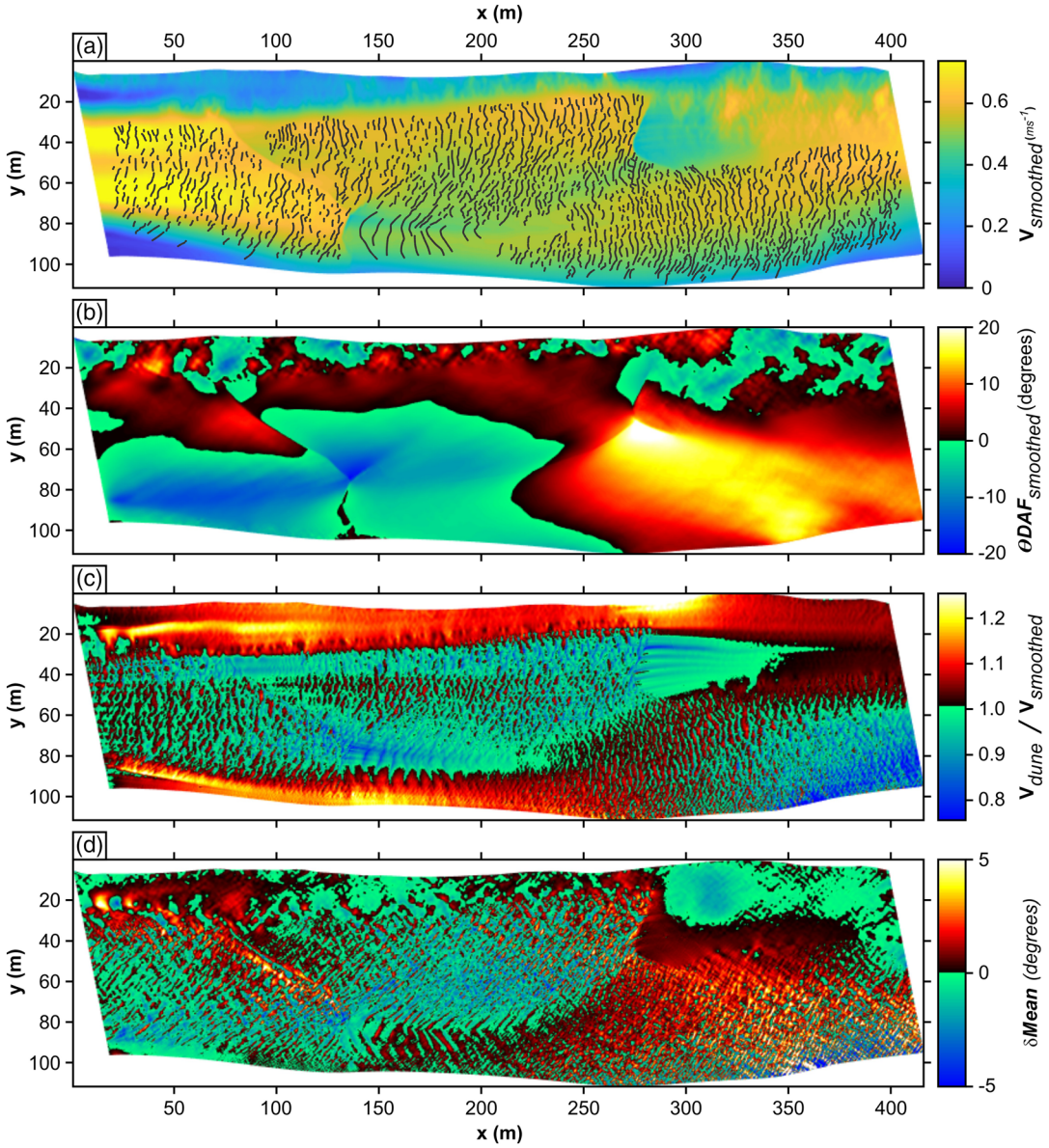

Figure 7. (a) Depth-averaged velocity magnitude for the *Smoothed DEM* simulation ($<V_{smoothed}>$), shown at fine resolution. Digitized dune crestlines are plotted as gray lines on this figure to give an indication of where the dune crestlines are located—it should be noted that these dunes are not present in the *Smoothed DEM* simulation but are shown in this panel for clarity. (b) Planform flow direction of depth-averaged velocities for the *Smoothed DEM* simulation ($\theta\ DAF_{smoothed}$), shown at fine resolution. Zero is downstream. Positive and negative directions are toward the true left and right banks, respectively. (c) Ratio of the depth-averaged velocity magnitude for the *Dune DEM* simulation ($<V_{dune}>$) to the depth-averaged velocity magnitude for the *Smoothed DEM* simulation ($<V_{smoothed}>$), shown at fine resolution. (d) Deviation between the depth-averaged flow directions for the *Dune DEM* simulation and the *Smoothed DEM* simulation ($\delta Mean$; calculated using (9)), shown at fine resolution.

similar to those found in laboratory studies by Allen (1968) and Talmon et al. (1995). Clearly, the dune leesides have a large effect on the near-bed flow structure. How this translates to flow and sediment transport at the coarser scales typically employed by 2-D morphodynamic models is investigated in the following sections.

3.3. Influence of Dunes on the Spatial Distribution of Flow

Figure 7 shows the planform patterns of the depth-averaged flow within the study reach. Depth-averaged velocity magnitude (shown for the *Smoothed DEM* simulations in Figure 7a) tends to be highest over the bar tops but also where channel width is constricted (e.g., near the inlet and outlet). Both banks are

characterized by consistently low velocity magnitudes, as are the troughs located downstream of each bar front. Planform flow directions (Figure 7b) illustrate clear flow divergence around bar tops, particularly in the upstream half of the reach. In downstream areas ($x > 250$ m), planform flow patterns become increasingly dominated by flow convergence into the bar trough on the true left of the channel. The ratio of the depth-averaged velocity magnitudes for the two simulations (Figure 7c) demonstrates the effect of dunes in reducing flow velocities over bar tops (green-blue areas in Figure 7c) and promoting increased velocities around bar edges and channel thalwegs (red-yellow areas in Figure 7c), by as much as 30%. The difference between the depth-averaged flow directions for the *Dune DEM* and *Smoothed DEM* simulations (quantified by the metric *δMean*; Figure 7d) when calculated for the fine-resolution model results indicates that dunes have a clear influence on local flow directions even in a depth-averaged sense. Despite the high degree of local variability in values of *δMean*, bar-scale patterns are evident in the influence of dunes on planform flow directions. For example, there is a visual match between the results shown in Figures 7b and 7d, which indicates that in the simulation that includes the effects of dunes, the deflection of flow toward the right bank in the upstream half of the reach and the movement of flow toward the left bank in downstream areas are both enhanced. The net influence of the dunes, which appears to be to enhance lateral flows and reduce velocities over bar tops, is likely to reflect the combined effect of enhanced roughness in shallow flow (bar tops) and topographic steering of the near-bed flow (see Figure 6).

The planform patterns of near-bed flow direction for the simulations using the *Smoothed DEM* and *Dune DEM* are shown in Figures 8a and 8b. In both cases, the broad spatial patterns are similar and characterized by channel-scale flow divergence in upstream areas and flow convergence, mainly toward the left bank, further downstream. The highest magnitude values of θ *NBF* are found in both simulations along bar fronts (e.g., inside the areas labeled i and ii in Figure 8b), indicating strong topographic steering of flow. Figures 8c and 8d show the difference between the near-bed flow directions for the *Dune DEM* and *Smoothed DEM* simulations (quantified by the metric *δBed*), plotted using the high resolution and 5 m spatially averaged results. The range of values for *δBed* (−20° to +20°) is similar in magnitude to the values of near-bed flow direction in both simulations ($\theta\ NBF_{dune}$ and $\theta\ NBF_{smoothed}$) illustrating that dune-scale bedforms have the potential to amplify significantly, or even reverse, the lateral direction of the near-bed flow. Results at a fine spatial resolution (e.g., Figure 8c) show a high degree of local spatial variability and are not obviously characterized by large-scale coherent patterns. Despite this, spatially averaged results (Figure 8d) illustrate clear bar-scale zonation of *δBed*. For example, over the bar top attached to the left bank (indicated by the label iv in Figure 8d), dunes promote near-bed flow up the bar (against the mean bed topography) and toward the center of the channel, while in the *Smoothed DEM* simulation the flow in this area is directed toward the left bank. In contrast, near-bed flow over the bar on the right of the channel (indicated by the label v in Figure 8d) is deflected toward the left bank by approximately 4–5° more in the *Dune DEM* simulation than in the *Smoothed DEM* simulation, which represents an amplification of the deviation from the downstream direction by approximately 25%. These trends indicate a potential role for dune leeside topography in steering the near-bed flow at scales larger than individual bedforms.

3.4. Influence of Dunes on Sediment Transport Directions

Displayed in Figure 9 is the sediment transport directions (calculated using Equations 11a–11d) for the *Smoothed DEM* (Figure 9a) and *Dune DEM* (Figure 9b) and the deviation between the two simulations (Figure 9c). While the overall directions of sediment transport across the DEM are comparable for the two simulations, there are subtle variations in transport direction when dunes are introduced. The close visual match between the patterns of near-bed flow direction (Figure 8a) and sediment transport direction (Figures 9a and 9b) suggest that gravitational deflection of sediment has a relatively small influence on sediment transport directions. Moreover, the similarity between patterns highlighted in the areas labeled iii, iv, and v in Figure 8d (for *δBed*) and the corresponding areas labeled i, ii, and iii in Figure 9c (for *δSed*) suggests that differences in the direction of sediment transport between the *Dune DEM* and *Smoothed DEM* are driven mainly by the influence of dunes on the near-bed flow (as opposed to the differences in gravitational deflection associated with dunes).

To investigate the effect of 3-D flow structure of sediment transport, the magnitude of the difference between the depth-averaged and near-bed flow directions is shown in Figure 10. Large differences between near-bed

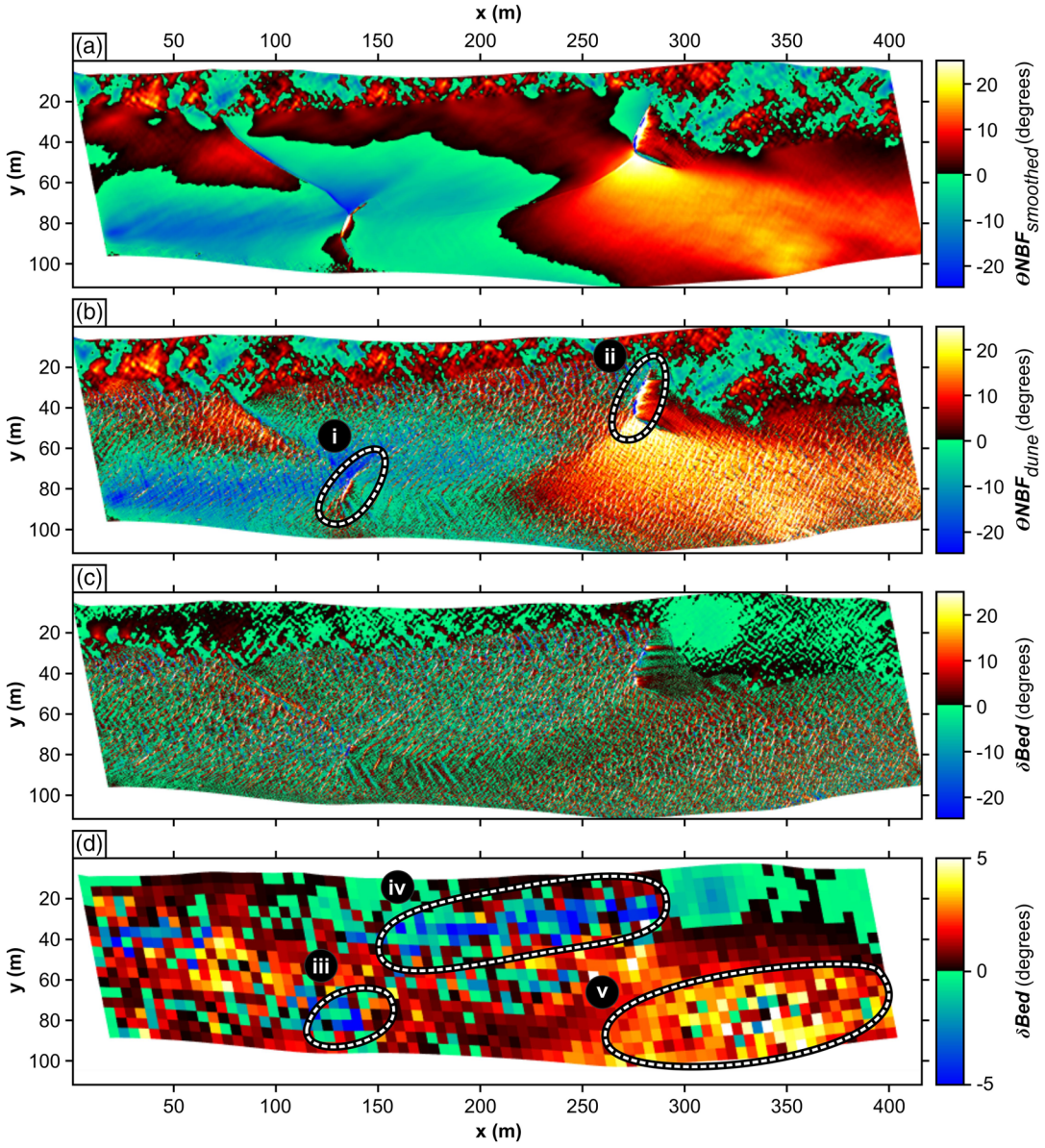

Figure 8. Planform flow direction of near-bed velocities for (a) the *Smoothed DEM* simulation ($\theta\ NBF_{smoothed}$) and (b) the *Dune DEM* simulation ($\theta\ NBF_{dune}$), shown at fine resolution. Zero is downstream. Positive and negative directions are toward the true left and right banks, respectively. (c and d) The deviation between the near-bed flow directions for the *Dune DEM* simulation and the *Smoothed DEM* simulation (δBed; calculated using Equation 10), plotted at fine resolution (c) and spatially averaged at 5 m resolution (d).

and depth-averaged flow directions are clearly associated with the location of bar fronts in the *Smoothed DEM* simulation (highlighted by labels i and iii in Figure 10). This illustrates the key role of bar-scale topographic forcing of flow structure as a control on the near-bed flow direction, which is what would be expected from a 2-D morphodynamic modeling perspective.

The general patterns in the deflection of the near-bed flow evident in Figure 10a are repeated and, in many areas, amplified by the presence of dunes (Figure 10b). For example, the median value of $\alpha Flow_{smoothed}$ is ~0.12°, while the median value of $\alpha Flow_{dune}$ is an order of magnitude larger (~1.05°). However, in specific areas the two simulations show very different trends. For example, on the left-hand edges of the channel over a distance of approximately 140 m (labeled ii in Figures 10b and 10c), dunes promote strong deflection of near-bed flow toward the center of the channel. In contrast, deflection of the near-bed flow over this bar top area is relatively weak in the *Smoothed DEM* simulation. Given that near bed flow directions in the *Dune*

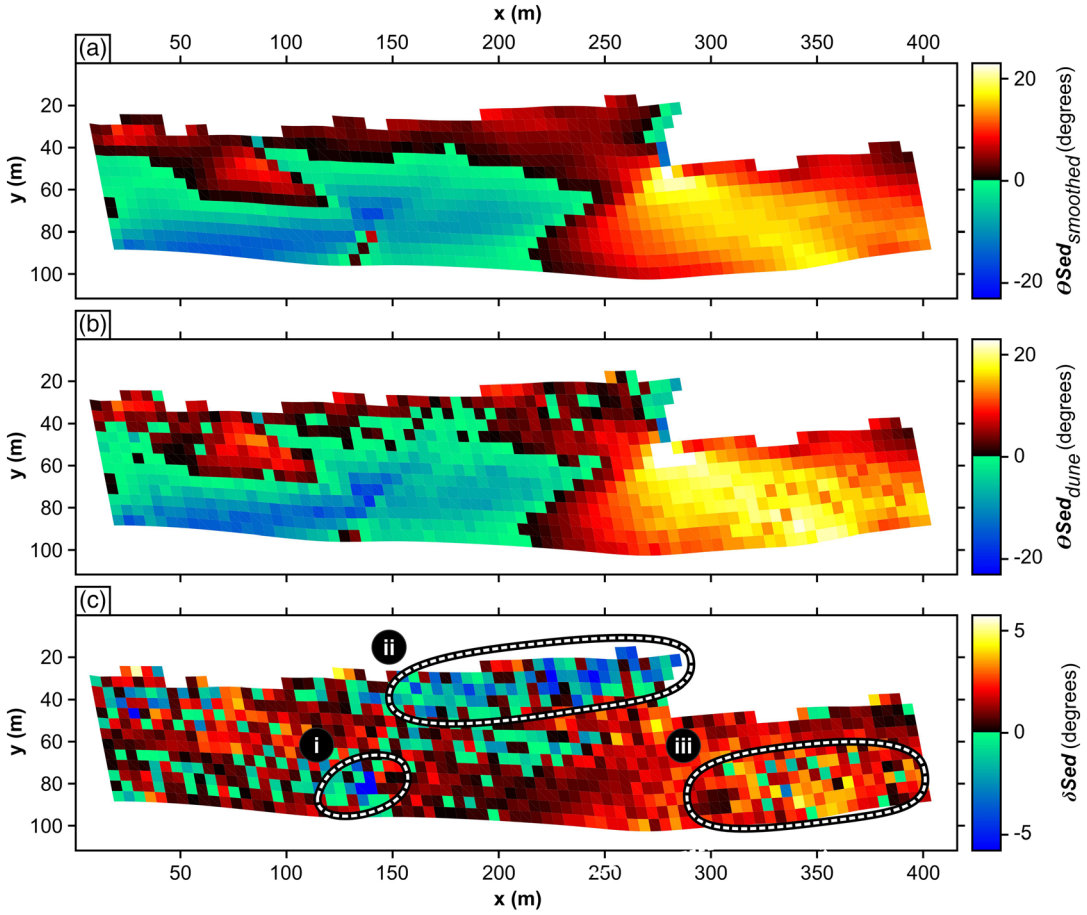

Figure 9. Planform sediment transport directions (calculated using Equations 11a–11d) for (a) the *Smoothed DEM* simulation ($\theta\ Sed_{smoothed}$) and (b) the *Dune DEM* simulation ($\theta\ Sed_{dune}$). Calculations were performed at fine resolution and then spatially averaged over a 5 m grid. Zero is downstream. Positive and negative directions are toward the true left and right banks, respectively. (c) Deviation between the sediment transport directions for the *Dune DEM* simulation and the *Smoothed DEM* simulation (δSed; calculated using Equation 12), spatially averaged at 5 m resolution. Results have been calculated and are shown, only for the sand-bedded regions of the channel.

DEM simulation are strongly affected by the local planform orientation of bedform troughs (Figure 6) it is likely that the degree to which dunes tend to amplify or reverse the deviation between the depth-averaged and near-bed flow directions should to be determined by the local planform orientation of bedform troughs. However, no systematic trend in crest orientations and the regions labeled in Figures 8–10 was found.

To observe the significance (or lack thereof) to the gravitational deflection of sediment by bed slopes, the magnitude of the difference between the near-bed flow and the sediment transport directions for the *Smoothed DEM* is shown in Figure 11a and *Dune DEM* (Figure 11b). The difference between Figures 11a and 11b (indexed by the metric δTop) is shown in Figure 11c and demonstrates the effect of including dune morphology. The patterns of topographic deflection of bed sediment in both simulations (Figures 11a and 11b) are controlled mainly by bar-scale morphology, with narrow zones of high topographic deflection corresponding directly to the location of bar fronts. The magnitude of the gravitational effect is similar for both simulations. However, despite the introduction of greater variability in the transverse bed slope in the presence of dunes, when spatially averaged at 5 m the magnitude of the difference in topographic deflections (Figure 11b) between the two simulations (indexed by δTop) is typically <1°, with no obvious spatial pattern or consistency (Figure 11c). Therefore, even in the presence of dunes, bar-scale topography still drives gravitational deflection of sediment.

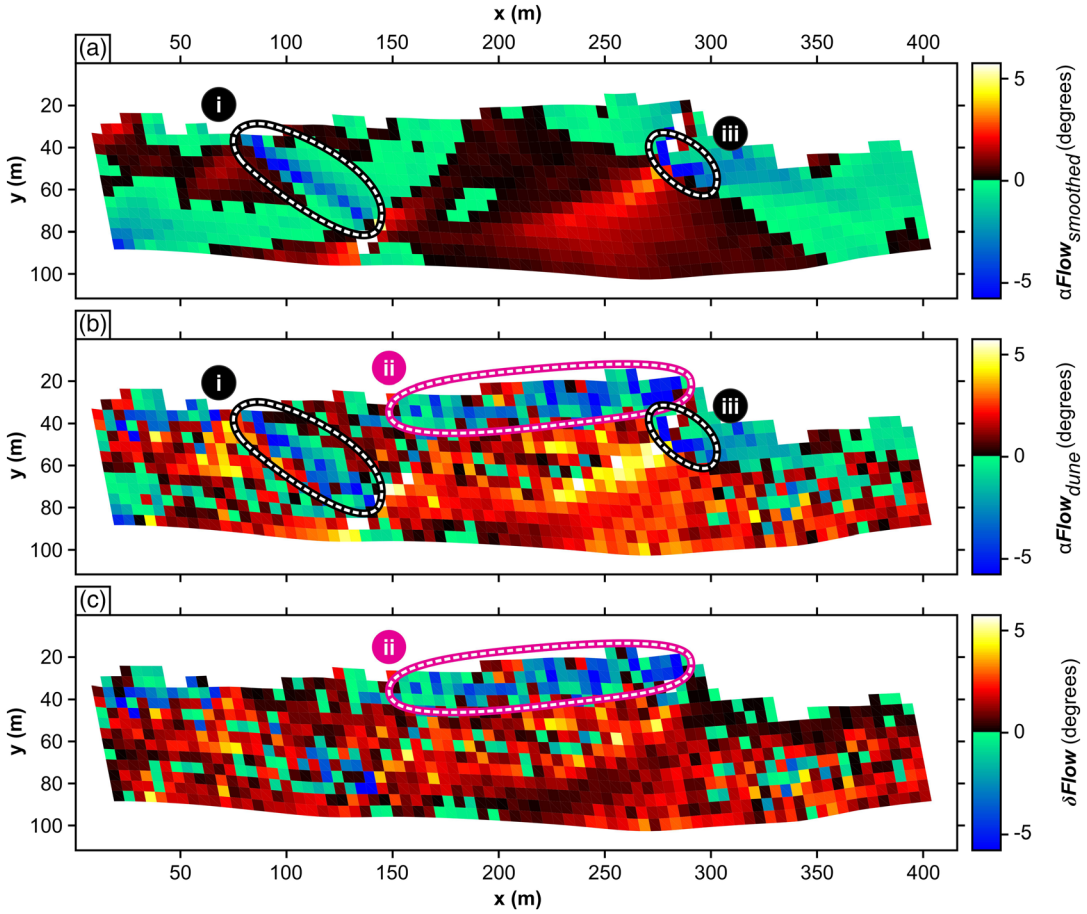

Figure 10. Planform patterns of the deviation between the near-bed flow direction and the depth-averaged flow direction calculated for (a) the *Smoothed DEM* simulation ($\alpha Flow_{smoothed} = \theta\ NBF_{smoothed} - \theta\ DAF_{smoothed}$) and (b) the *Dune DEM* simulation ($\alpha Flow_{dune} = \theta\ NBF_{dune} - \theta\ DAF_{dune}$), shown at 5 m resolution for the sand bed portion of the reach. (c) Planform patterns of the difference ($\delta Flow$; calculated using Equation 13) between values of ($\theta\ NBF - \theta\ DAF$) for the *Dune DEM* and *Smoothed DEM* simulations, shown at 5 m resolution for the sand bed portion of the reach.

4. Discussion

The results outlined in section 3 show that (i) the majority (>60%) of dune orientations are oblique to their upstream flow direction (Figure 6); (ii) there is substantial steering of flow in dune troughs, with the majority of deviations (relative to the flow just upstream of the dune crest) peaking at ~+50° (Figure 6) and oriented toward the left bank; and (iii) depth-averaged velocities are up to 30% lower over bar tops and 30% higher in thalwegs (Figure 7) for simulations that represent dunes compared with simulations where dunes are neglected. Results also illustrate that dunes have significant effects (identified by spatial averaging of model results) on flow and on inferred sediment transport at spatial scales larger than individual bedforms (Figure 8). With spatial averaging employed, spatially coherent trends can be seen when comparing between simulations (δ symbol variables in Figures 8–11) and when looking at individual variables of a simulation (θ symbol variables in Figures 8–11). For example, Figures 9 and 10 identify coherent regions where flow and sediment transport directions (relative to the dominant downstream flow direction) have been reversed or amplified by the presence of dunes. In contrast, Figure 11 demonstrates that dunes may have limited effects on the gravitational deflection of sediment transport. To relate these variables together within a single framework, the following section examines the relative importance of each variable to the overall difference in sediment transport directions between the two simulations (the measure δSed).

4.1. Interpretation of Results

The results presented above illustrate significant differences in flow and sediment transport directions in the two simulations conducted using the *Dune DEM* and *Smoothed DEM*. Equations 5–10 allow quantification of

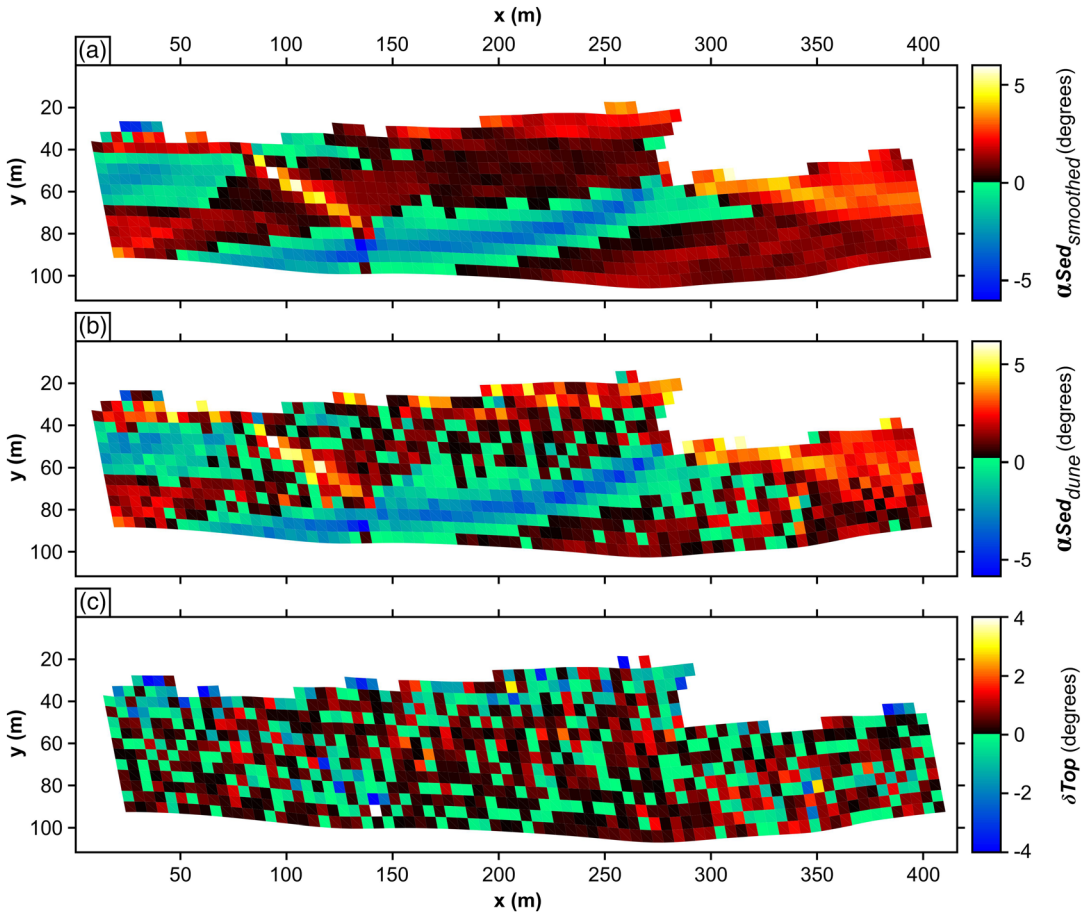

Figure 11. Planform patterns of the deviation between the sediment transport direction and the near-bed flow direction calculated for (a) the *Smoothed DEM* simulation ($\alpha Sed_{smoothed} = \theta\ Sed_{smoothed} - \theta\ NBF_{smoothed}$) and (b) the *Dune DEM* simulation ($\alpha Sed_{dune} = \theta\ Sed_{dune} - \theta\ NBF_{dune}$), shown at 5 m resolution for the sand bed portion of the reach. (c) Planform patterns of the difference (δTop; calculated using Equation 14) between values of ($\theta\ Sed - \theta\ NBF$) for the *Dune DEM* and *Smoothed DEM* simulations, shown at 5 m resolution for the sand bed portion of the reach.

the relative contributions to δSed, resulting from differences in the depth-averaged and near-bed flow and the gravitational deflection of sediment in the presence and absence of dunes. For example, Figure 12 displays the cumulative frequency distribution of the difference between sediment transport directions calculated for the *Dune DEM* and *Smoothed DEM* simulations (δSed). Distributions are also shown for (i) differences in the depth-averaged flow direction between the simulations (indexed by $\delta Mean/\delta Sed$); (ii) differences in the deviation between the near-bed flow, and the depth-averaged flow directions between the simulations (indexed by $\delta Flow/\delta Sed$); and (iii) differences in the strength of the transverse slope effect (indexed by $\delta Top/\delta Sed$). Each point in these distributions is derived from the mean values of the model variables calculated within a single 5 m grid cell (i.e., following spatial averaging of the high resolution CFD results). It should also be noted that $\delta Sed = \delta Mean + \delta Flow + \delta Top$ and that the metrics $\delta Flow$ and δTop represent the difference between the results of the simulations carried out using the *Dune* and *Smoothed* DEMs for the two components of the deviation between the depth-averaged flow and sediment transport directions illustrated in Figure 1 (i.e., $\alpha Flow$ and αSed).

The distributions in Figure 12 show that δSed is positive over approximately 75% of the model domain, indicating that overall, the presence of dunes tends to deflect sediment toward the left bank relative to the sediment transport direction for the *Smoothed DEM*. The magnitude of $\delta Flow/\delta Sed$ is approximately 3 times the magnitude of $\delta Mean/\delta Sed$ over much of the distribution, although $\delta Mean/\delta Sed$ does make a positive contribution to δSed on average ($\delta Mean/\delta Sed$ values are positive in 66% of locations). The distribution of $\delta Top/\delta Sed$ is approximately symmetrical with a large area of the domain characterized by low values. These distributions indicate that the differences in depth-averaged flow directions between the two simulations make a

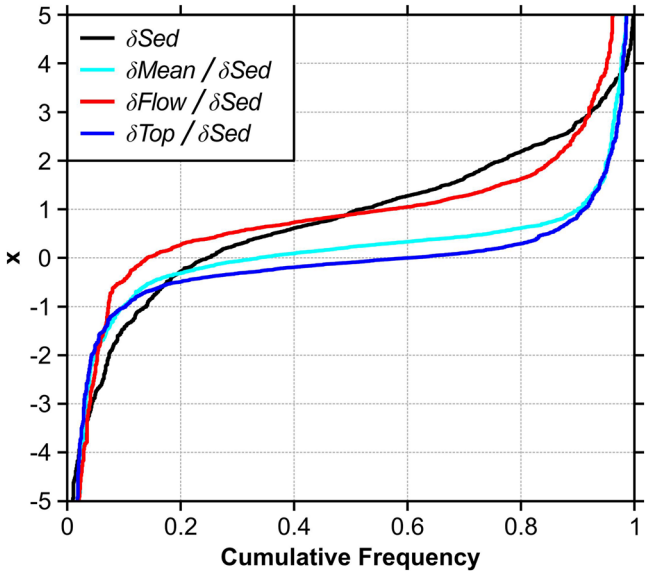

Figure 12. Cumulative frequency distribution for δSed (measured in degrees, plotted on the x axis) and the relative contributions to δSed from $\delta Mean$ (Equation 9), $\delta Flow$ (Equation 13), and δTop (Equation 14). The x axis shows the cumulative frequency. Results are shown for the model results spatially averaged at 5 m resolution.

relatively small contribution to the differences in sediment transport directions. Differences between near-bed and depth-average flow directions is the dominant control on sediment transport directions in the *Dune DEM*. The overall effects of dunes on topographic deflection of sediment are relatively small, except at the extreme tails of the distribution shown in Figure 12.

To compare the results of these simulations with values that are more indicative of conditions within 2-D depth-averaged morphodynamic models (that do not represent dunes explicitly), the net deviation between the sediment transport direction and depth-averaged flow direction results for the *Smoothed DEM* simulation was calculated. These values are plotted on Figure 13a as "$\alpha Flow_{Smoothed} + \alpha Sed_{Smoothed}$," against δSed. Several previous studies have highlighted that 2-D models are sensitive to the parameterization of secondary circulation effects and gravitational deflection of sediment (Nicholas et al., 2013; Schuurman et al., 2013), both of which contribute to $\alpha Flow_{Smoothed} + \alpha Sed_{Smoothed}$. Consequently, it is pertinent to consider the extent to which dunes tend to amplify or dampen these effects.

Figure 13a plots model results in the context of four quadrants. In Quadrants Q1 and Q3, δSed and $\alpha Flow_{Smoothed} + \alpha Sed_{Smoothed}$ have the same sign, indicating that dunes tend to deflect sediment in the same direction as the deviation between the sediment transport and depth-averaged flow directions for the *Smoothed DEM* simulation; that is, in these cases dunes amplify the deflection seen in the *Smoothed DEM* simulation. In contrast, in Quadrants Q2 and Q4, the effect of dunes is to steer sediment in the opposite direction to the deviation between the sediment transport and depth-averaged flow directions for the *Smoothed DEM* simulation. Figure 13b illustrates the spatial distribution of data points in these four quadrants. Approximately half (56%) of the study reach is associated with data in Q1, indicating that sediment transport in the presence of dunes deflects sediment toward the left bank *and* in the same direction as the steering of sediment transport (relative to the depth-averaged flow) in the *Smoothed DEM* simulation. In contrast, approximately 35% of the study reach is associated with situations where dunes deflect sediment in the *opposite* direction to the steering of sediment transport (relative to the depth-averaged flow) in the *Smoothed DEM* simulation. Figure 13b illustrates a strong spatial coherence to these tendencies. In the area labeled i in Figure 13b, sediment transport in the *Smoothed DEM* simulation is steered toward the left bank, yet dunes tend to steer sediment in the opposite direction and up the bar face (i.e., Q4). In contrast, the area labeled ii in Figure 13b is characterized by strong steering of the near-bed flow and/or topographic deflection of sediment toward the right bank in the *Smoothed DEM*, while the presence of dunes in this area tends to deflect sediment transport in the opposite direction. Moreover, in the case of all four quadrants, the magnitude of δSed is, on average, approximately twice the value of when dunes were not present ($\alpha Flow_{Smoothed} + \alpha Sed_{Smoothed}$). This difference suggests that failure of 2-D morphodynamic models to represent the effects of dunes on near-bed flow and sediment transport will lead to significant and systematic differences in sediment transport direction between model and reality.

Because 2-D morphodynamic models operate at relatively coarse spatial resolutions and do not represent variations in bed topography that are associated with dunes and other alluvial bedforms, they are likely to underestimate spatial variability in flow velocities. Moreover, this will have implications for the calculation of sediment transport rates over a range of scales (e.g., Ferguson, 2003; Furbish et al., 2012). To try and quantify these effects for our present example, a simple metric of sediment transport (velocity magnitude raised to the power five), based on the Engelund and Hansen (1967) sediment transport formulae, is used. The effects of neglecting dune-scale variations in flow can be quantified at a resolution relevant to 2-D morphodynamic modeling (e.g., 5 m in the case of the present study reach) by calculating the mean value of this sediment transport rate within each 5 m grid cell using the high resolution (8 cm) model output and dividing this by the equivalent metric derived using coarse-resolution (5 m) spatially averaged velocities. The spatial

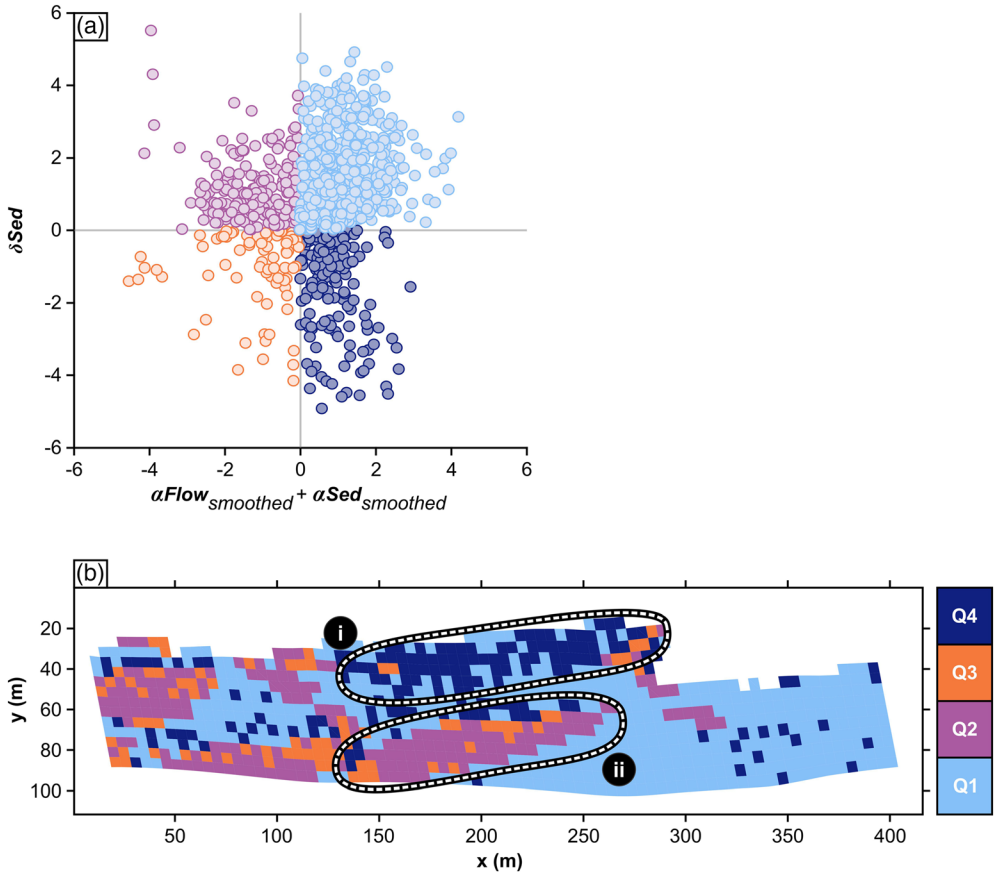

Figure 13. (a) Scatter plot of the combined deviation between sediment transport and depth-averaged flow directions for the *Smoothed DEM* ($\alpha Flow_{smoothed} + \alpha Sed_{smoothed}$) plotted against the difference in sediment transport directions between the *Dune DEM* and *Smoothed DEM* simulations (δSed). This scatter plot illustrates the magnitude of the net effect of dunes compared to magnitude of the deviation between the depth-averaged flow and sediment transport directions in the absence of dunes. Data are segmented into four quadrants. Points in Q1 and Q3 indicate areas where dunes deflect sediment transport in the same direction as the deviation between the mean flow and sediment transport in the absence of dunes (i.e., the addition of dunes can be inferred to amplify tendencies evident in the smoothed DEM simulation. (b) The planform distribution of data points for these four quadrants. Areas i and ii highlight regions of spatially consistent Q2, along a bar edge, and Q4, along a bar top near the left bank. Q1 dominates the latter third of the DEM, where the presence of dunes has amplified the deflection of flow from true right to left.

patterns of this ratio derived using near-bed flow velocities (a) and depth-averaged flow velocities (c) are shown in Figure 14. The order of magnitude difference in the values shown in Figure 14a compared with Figure 14c demonstrates that neglecting variations in near-bed velocity associated with dunes has the potential to substantially affect sediment transport rates calculated (Figure 14a).

The effects of neglecting dunes can also be quantified by calculating the sediment transport metric using the mean velocity values within each 5 m grid cell derived from the *Dune DEM* simulation, divided by the metric derived from the *Smoothed DEM* simulation (Figures 14b and 14d). As 2-D morphodynamic models use sediment transport formulae (e.g., Engelund-Hansen) based on depth-averaged flow variables, on which the dune-scale topography has a more limited effect (e.g., in the 3-D simulations reported herein), the neglect of dune-scale topography has little effect on sediment transport rates (when measured using the simple metric employed here—see Figure 14c). In the context of 2-D morphodynamic modeling, the main effect of neglecting dunes on this sediment transport rate is associated with redistribution of the flow, which reduces velocity over bar tops and enhances flow and sediment transport in thalwegs and along the channel margins. This effect is equally significant in the context of both the depth-averaged and near-bed flow (Figure 14b vs. Figure 14d).

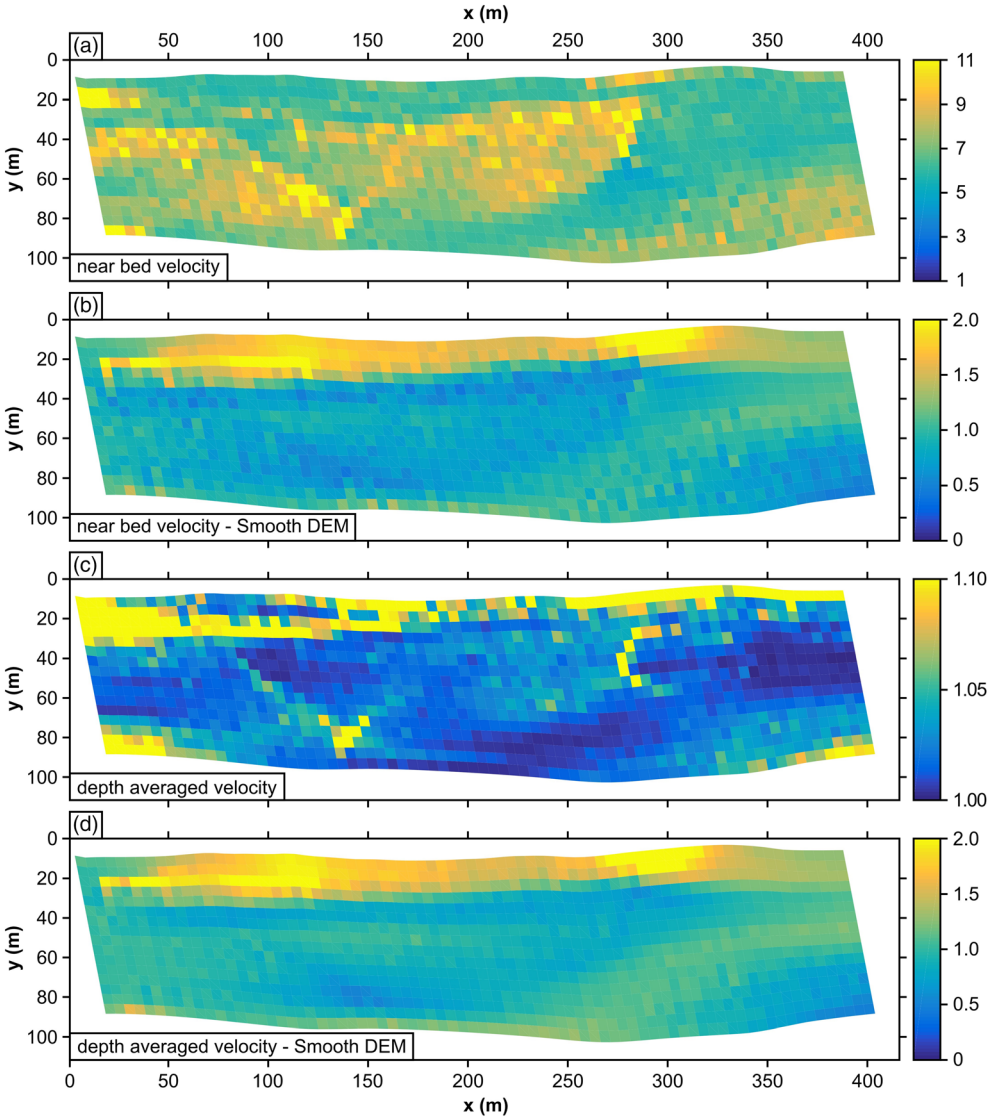

Figure 14. Ratios of sediment transport rates. To assess how spatial variability of flow could affect sediment transport rates, near-bed velocity (a, b) and depth-averaged velocity (c, d) magnitudes were raised to the power 5 (Engelund & Hansen, 1967). For Panels (a) and (c) this sediment transport rate was calculated at the 8 cm CFD grid resolution, then averaged to 5 m, and divided by a sediment transport rate calculated from the corresponding 5 m averaged velocity magnitude. This comparison demonstrates an order of magnitude difference in sediment transport rate when using near-bed flow velocities (a) compared to using depth-averaged velocities (c). Panels (b) and (d) have the same calculation of sediment transport rate at the CFD resolution, but are divided by the equivalent metric from smooth DEM simulation. Panels (b) and (d) demonstrate similar magnitudes and spatial distributions, with the depth-averaged case (d) smoother than the near-bed flow case (b). Panels (b) and (d) therefore demonstrate that redistribution of the flow away from bar tops to thalwegs is equally significant for near-bed (b) and depth-averaged (d) flow.

4.2. Implications

The results presented herein demonstrate that dunes can either amplify or suppress the deflection of sediment via steering of the near-bed flow, as a result of which it may be difficult to produce a simple method of accounting for dunes in 2-D morphodynamic models. Deviations between the depth-averaged and near-bed flow are incorporated in depth-averaged models as secondary circulation effects, often modeled as a function of streamline curvature (Struiksma et al., 1985). However, the simple (straight) morphology of the current study reach results in low planform curvature so that values of $\alpha Flow$ for the simulations reported herein are driven by topographic steering of the near-bed flow (e.g., by bar fronts or dunes aligned oblique to the mean flow). This may indicate that, particularly in the absence of strong channel planform

curvature, there is a need to develop new parameterizations for use within depth-averaged models of the effects of near-bed topography on the vertical distribution of flow velocity.

There are approaches for predicting the spatial distribution of dune height within depth-averaged morphodynamic models (e.g., Giri et al., 2008). The results presented herein suggest that dune height (or more pertinently, roughness) will affect the spatial distribution of sediment transport rates through their effect on the mean flow (Figure 14c and 14d). When dunes are included, the majority of the differences in sediment transport directions is due to the effects of dunes on steering of near-bed flow ($\delta Flow$, Figure 12). To account for these effects, new approaches for predicting dune orientation are needed that will provide a basis for deriving improved parameterizations of the deviation between the depth-averaged and near-bed flow. However, this task is difficult to accomplish a priori (e.g., Weij, 2012), as dune orientation is often a product of the interplay between bed slope, spatially nonhomogeneous sediment transport rates (Rubin, 2012; Terwisscha van Scheltinga et al., 2020; Unsworth et al., 2016; Weij, 2012), and the interaction that dunes have on the mean flow field.

The relatively small contribution of gravitational deflection of sediment by local (dune-scale) bed slopes to the differences between sediment transport directions for the *Dune DEM* and *Smoothed DEM* simulations is noteworthy, particularly given that the analysis conducted using Equations 11a–11d was intended to maximize the potential magnitude of this effect. It is important to clarify that sediment transport directions estimated herein (using Equations 11a–11d) are *only* for bedload transport. While dunes are nearly always responsible for suspending some sand (Kuhnle & Wren, 2009; Naqshband et al., 2014; Wren et al., 2007), the effect of gravitational deflection (measured by δTop) on suspended material remains highly uncertain (Talmon & Wiesemann, 2006). Moreover, the conditions considered herein are more representative of the critical threshold of motion, since they evaluate the maximum likely contribution of transverse slope effects. At higher flow stages, and where a significant proportion of sediment moves in suspension, the effects of gravitational deflection are likely to be weaker than those reported herein (cf. Baar et al., 2018). This suggests that while parameterization of gravitational deflection due to transverse slope effects within depth-averaged models remains a key control on simulated channel morphology (Baar et al., 2019; Nicholas, 2013; Schuurman et al., 2013), improved parameterization of these effects may not necessitate explicit representation of the effects of dunes on δTop within such models. However, this conclusion may reflect, in part, the nature of the analysis conducted herein, which has been designed to represent the calculations performed by depth-averaged morphodynamics models, rather than the physical controls on sediment transport at fine (subdecimeter) spatial and temporal scales. Similar conclusions can be drawn in relation to the analysis presented in Figure 14 that indicates that the neglect of spatial variations in velocity associated with dunes will have a limited effect on sediment transport rates calculated in 2-D morphodynamic models, where these transport rates are based on formulae that utilize depth-averaged velocities. Full account within such models of the potential effects of dunes on sediment transport would necessitate the development of theory that accounts for the controls on near-bed turbulent sediment transport (Furbish et al., 2012) and its relationship to the depth-averaged flow and local bed morphology.

One of the primary limitations of the present analysis is that the sediment transport directions calculated herein do not include the effects of avalanching on the lee faces of bars or dunes. Flow reworking of sediment on the lee face is approximated by the present analysis but notably does not include the important contribution of turbulence-derived sediment transport events in the leeside (Nabi et al., 2015; Schmeeckle, 2014). Lee face reworking by the flow can form a substantial proportion of the sediment transport directions along the slip face, especially when the bedform crests and troughs are oblique to the mean flow direction (Sieben & Talmon, 2011; Terwisscha van Scheltinga et al., 2020; Unsworth et al., 2016). The contribution of lee face reworking has mostly only been quantified in the field for eolian environments (e.g., Nield et al., 2017; Pelletier et al., 2015) and has not yet received detailed field study in aqueous unidirectional flows where there are 2-D and 3-D bedforms migrating over lateral slopes.

Cisneros et al. (2020) recently demonstrated that dune leesides in many of the world's larger rivers tend to have low-angle lee slopes. Such low-angle dunes produce smaller flow separation zones or no permanent flow separation at all (Best & Kostaschuk, 2002; Lefebvre & Winter, 2016) resulting in reduced form drag (Kwoll et al., 2016). Crestline obliqueness effects on near-bed velocity directions is produced in the

present work, but how leeside flow deflection is then changed with a lower leeside slope angles or composite leesides commonly found in larger rivers is an avenue of future research.

5. Conclusions

This paper reports on the application of a 3-D CFD model to simulate time-averaged flow patterns within a 400 m reach of the sand-bedded South Saskatchewan River, Canada. Two simulations were conducted using high-resolution DEMs with and without dunes. The differences between these simulations are discussed in relation to 2-D morphodynamic modeling. The main findings are the following:

1. The presence of dunes promotes redistribution of flow away from shallow bar tops toward the channel margins. This effect reduces bar top velocities by up to 30% and promotes a concomitant increase in bank edge velocities.
2. For depth-averaged flow, dunes amplify the dominant patterns of cross-stream flow induced by the bar-scale channel morphology.
3. Dunes promote substantial local variability in near-bed flow directions, even when averaged up to the scale at which 2-D morphodynamic models operate. In many areas, near-bed flow is steered by dune troughs which are oriented oblique to the downstream flow direction; this leads to differences in near-bed flow directions between simulations with and without dunes that exceed 45° in some locations.
4. Spatial averaging of high-resolution model results indicates that the effects of dunes on flow and sediment transport directions are evident at spatial scales coarser than the largest dunes and up to the scale of individual channel-scale bar forms. Parameterization of this subgrid-scale effect for morphodynamic models requires prediction of dune crestline orientation.
5. Significant differences between depth-averaged and near-bed flow directions are evident in simulations that use a *Smoothed DEM* (i.e., with dune bedforms removed). These differences reflect topographic steering of the flow (e.g., by bar fronts) in the absence of significant planform curvature, rather than the effects of secondary circulation driven by planform curvature.
6. Sediment transport patterns inferred using theory implemented in depth-averaged morphodynamic models suggests that gravitational deflection of sediment is controlled by bar-scale topography. Dune-scale topography promotes local variability in such gravitational deflection, but this effect is not associated with a coherent signal at spatial scales larger than individual dunes. The dominant effect of dunes on sediment transport directions is through their influence on near-bed flow directions, with a secondary effect linked to their impact on the depth-averaged flow.

These results have implications for the parameterization of flow and sediment transport processes in depth-averaged morphodynamic models. Specifically, they indicate that secondary circulation schemes based on streamline curvature may fail to represent controls on the deviation between depth-averaged and near-bed flow directions. Improvements in the realism of depth-averaged flow models may only be achieved through the development of new approaches for predicting the spatial distribution of bedform height and orientation.

Data Availability Statement

Project data are stored in, and available from, the UK Centre for Ecology and Hydrology (http://eidc.ceh.ac.uk).

Acknowledgments

P. J. A., A. P. N., D. R. P., and G. S. S. thank the UK Natural Environment Research Council (NERC) for grants NE/L00738X/1, NE/L005662/1, NE/L00450X/1, and NE/L005441/1 that funded this work. Vance and Janine Ylioja kindly gave us access to their land and boat launch, while Bill Vavra generously provided storage facilities and access to his land. Bob and Sandy Stephenson at the Irrigation Motel in Outlook provided invaluable assistance and logistical support. Image processing was performed using Pix4Dmapper software under an educational license (Pix4D SA, Switzerland). Simulations were run on the Exeter University High-Performance Cluster ISCA. Professor Gavin Tabor and Dr. Recep Kahraman are thanked for their support with OpenFOAM. Dr. Tim Maddux is thanked for supplying his dune morphology and flow data for model validation. We thank the Editors, Dr. Alice Lefebvre, and two anonymous reviewers for very helpful and constructive reviews.

References

Abad, J. D., Frias, C. E., Buscaglia, G. C., & Garcia, M. H. (2013). Modulation of the flow structure by progressive bedforms in the Kinoshita meandering channel. *Earth Surface Processes and Landforms*, *38*(13), 1612–1622. https://doi.org/10.1002/esp.3460

Allen, J. R. L. (1968). *Current ripples: Their relation to patterns of water and sediment motion*. Amsterdam: North-Holland Pub. Co. https://www.cambridge.org/core/journals/geological-magazine/article/john-r-l-allen-1968-current-ripples-their-relation-to-patterns-of-water-and-sediment-motion-xiii-433-p-445-figs-north-holland-publishing-company-amsterdam-price-12-12s-hfl108-3000/8292E307D09AF3F0EB9303A77137DC6F

Antoniazza, G., Bakker, M., & Lane, S. N. (2019). Revisiting the morphological method in two-dimensions to quantify bed-material transport in braided rivers. *Earth Surface Processes and Landforms*, *44*(11), 2251–2267. https://doi.org/10.1002/esp.4633

Apsley, D. D., & Stansby, P. K. (2008). Bed-load sediment transport on large slopes: Model formulation and implementation within a RANS solver. *Journal of Hydraulic Engineering*, *134*(10), 1440–1451. https://doi.org/10.1061/(ASCE)0733-9429(2008)134:10(1440)

Baar, A. W., Boechat Albernaz, M., van Dijk, W. M., & Kleinhans, M. G. (2019). Critical dependence of morphodynamic models of fluvial and tidal systems on empirical downslope sediment transport. *Nature Communications*, *10*(1), 4903. https://doi.org/10.1038/s41467-019-12753-x

Baar, A. W., de Smit, J., Uijttewaal, W. S. J., & Kleinhans, M. G. (2018). Sediment transport of fine sand to fine gravel on transverse bed slopes in rotating annular flume experiments. *Water Resources Research*, *54*, 19–45. https://doi.org/10.1002/2017WR020604

Best, J., & Kostaschuk, R. (2002). An experimental study of turbulent flow over a low-angle dune. *Journal of Geophysical Research: Oceans*, *107*(C9), 3135. https://doi.org/10.1029/2000JC000294

Best, J. L. (2005). The fluid dynamics of river dunes: A review and some future research directions. *Journal of Geophysical Research: Earth Surface*, *110*, F04S02. https://doi.org/10.1029/2004jf000218

Blanckaert, K. (2010). Topographic steering, flow recirculation, velocity redistribution, and bed topography in sharp meander bends. *Water Resources Research*, *46*, W09506. https://doi.org/10.1029/2009WR008303

Bradbrook, K. F., Lane, S. N., & Richards, K. S. (2000). Numerical simulation of three-dimensional, time-averaged flow structure at river channel confluences. *Water Resources Research*, *36*(9), 2731–2746. https://doi.org/10.1029/2000WR900011

Bridge, J. S. (1993). The interaction between channel geometry, water flow, sediment transport and deposition in braided rivers. In J. B. Best, & C. S. Bristrow (Eds.), *Braided rivers*, *Special Pub* (Vol. 75, pp. 13–71). London: Geological Society Publishing House. https://doi.org/10.1144/GSL.SP.1993.075.01.02

Cant, D. J. (1976). Braided stream sedimentation in the South Saskatchewan River. PhD thesis, McMaster University. https://macsphere.mcmaster.ca/handle/11375/17504

Cant, D. J., & Walker, R. G. (1978). Fluvial processes and facies sequences in the sandy braided South Saskatchewan River. *Sedimentology*, *25*(5), 625–648. https://doi.org/10.1111/j.1365-3091.1978.tb00323.x

Chavarrías, V., Schielen, R., Ottevanger, W., & Blom, A. (2019). Ill-posedness in modelling two-dimensional morphodynamic problems: Effects of bed slope and secondary flow. *Journal of Fluid Mechanics*, *868*, 461–500. https://doi.org/10.1017/jfm.2019.166

Cisneros, J., Best, J., van Dijk, T., de Almeida, R. P., Amsler, M., Boldt, J., et al. (2020). Dunes in the world's big rivers are characterized by low-angle lee-side slopes and a complex shape. *Nature Geoscience*, *13*(2), 1–7.

Dietrich, W. E., Smith, J. D., & Dunne, T. (1979). Flow and sediment transport in a sand bedded meander. *The Journal of Geology*, *87*(3), 305–315. https://doi.org/10.1086/628419

Doré, A., Bonneton, P., Marieu, V., & Garian, T. (2016). Numerical modeling of subaqueous sand dune morphodynamics. *Journal of Geophysical Research: Earth Surface*, *121*, 565–587. https://doi.org/10.1002/2015JF003689

Drake, T. G., Shreve, R. L., Dietrich, W. E., Whiting, P. J., & Leopold, L. B. (1988). Bedload transport of fine gravel observed by motion-picture photography. *Journal of Fluid Mechanics*, *192*, 193–217. https://doi.org/10.1017/S0022112088001831

Engel, F. L., & Rhoads, B. L. (2016). Three-dimensional flow structure and patterns of bed shear stress in an evolving compound meander bend. *Earth Surface Processes and Landforms*, *41*(9), 1211–1226. https://doi.org/10.1002/esp.3895

Engelund, F. (1974). Flow and bed topography in channel bends. *Journal of the Hydraulics Division*, *100*, 10963.

Engelund, F., & Hansen, E. (1967). *A monograph on sediment transport in alluvial streams*. Copenhagen: Technical University of Denmark.

Ferguson, R. I. (2003). The missing dimension: Effects of lateral variation on 1-D calculations of fluvial bedload transport. *Geomorphology*, *56*(1–2), 1–14.

Francalanci, S., & Solari, L. (2008). Bed-load transport equation on arbitrarily sloping beds. *Journal of Hydraulic Engineering*, *134*(January), 110–115. https://doi.org/10.1061/(ASCE)0733-9429(2008)134:1(110)

French, J. R. (2010). Critical perspectives on the evaluation and optimization of complex numerical models of estuary hydrodynamics and sediment dynamics. *Earth Surface Processes and Landforms*, *35*(2), 174–189. https://doi.org/10.1002/esp.1899

Furbish, D., Haff, P., Roseberry, J., & Schmeeckle, W. (2012). A probabilistic description of the bed load sediment flux: 1. Theory. *Journal of Geophysical Research*, *117*, F03031. https://doi.org/10.1029/2012JF002352

Giri, S., & Shimizu, Y. (2006). Numerical computation of sand dune migration with free surface flow. *Water Resources Research*, *42*, W10422. https://doi.org/10.1029/2005WR004588

Giri, S., Van Vuren, S., Ottevanger, S., & Sieben, K. (2008). A preliminary analysis of bedform evolution in the Waal during the 2002–2003 flood event using Delft3D. In J. L. Best (Ed.), *Proceedings of the Marine and River Dune Dynamics* (pp. 141–148). Leeds: University of Leeds.

Hardy, R. J., Lane, S. N., & Yu, D. (2011). Flow structures at an idealized bifurcation: A numerical experiment. *Earth Surface Processes and Landforms*, *36*(15), 2083–2096. https://doi.org/10.1002/esp.2235

Ikeda, S. (1982). Lateral bed load transport on side slopes. *Journal of the Hydraulics Division, ACSE*, *108*, 1369–1373.

Iwasaki, T., Shimuzu, Y., & Kimura, I. (2016). Numerical simulation of bar and bank erosion in a vegetated floodplain: A case study in the Otofuke River. *Advances in Water Resources*, *93*, 118–134. https://doi.org/10.1016/J.ADVWATRES.2015.02.001

Jasak, H. (1996). Error analysis and estimation for the finite volume method with applications to fluid flows. PhD thesis, Department of Mechanical Engineering Imperial College of Science, Technology and Medicine.

Karim, F. (1995). Bed configuration and hydraulic resistance in alluvial-channel flows. *Journal of Hydraulic Engineering*, *121*(1), 15–25. https://doi.org/10.1061/(ASCE)0733-9429(1995)121:1(15)

Kleinhans, M. G., Jagers, H. R. A., Mosselman, E., & Sloff, C. J. (2008). Bifurcation dynamics and avulsion duration in meandering rivers by one-dimensional and three-dimensional models. *Water Resources Research*, *44*, W08454. https://doi.org/10.1029/2007WR005912

Koch, F, Flokstra, C. (1981). Bed level computations for curved alluvial channels. In: *Proc. XIXth IAHR congress,* 2–7 February, 1981, New Delhi, India, vol. 2; 1981. p. 357–88.

Konsoer, K. M., Rhoads, B. L., Best, J. L., Langendoen, E. J., Abad, J. D., Parsons, D. R., & Garcia, M. H. (2016). Three-dimensional flow structure and bed morphology in large elongate meander loops with different outer bank roughness characteristics. *Water Resources Research*, *52*, 9621–9641. https://doi.org/10.1002/2016WR019040

Kuhnle, R. A., & Wren, D. G. (2009). Size of suspended sediment over dunes. *Journal of Geophysical Research*, *114*, F02020. https://doi.org/10.1029/2008JF001200

Kwoll, E., Venditti, J. G., Bradley, R. W., & Winter, C. (2016). Flow structure and resistance over subaquaeous high- and low-angle dunes. *Journal of Geophysical Research: Earth Surface*, *121*, 545–564. https://doi.org/10.1002/2015JF003637

Lane, S., & Richards, K. (2001). The "validation" of hydrodynamic models: Some critical perspectives. In M. Anderson & P. Bates (Eds.), *Model validation: Perspectives in hydrological science* (pp. 413–438). Chichester: Wiley.

Lane, S. N., Bradbrook, K. F., Richards, K. S., Biron, P., & Roy, G. (1999). The application of computational fluid dynamics to natural river channels: Three-dimensional versus two-dimensional approaches. *Geomorphology*, *29*(1–2), 1–20. https://doi.org/10.1016/S0169-555X(99)00003-3

Lane, S. N., Hardy, R. J., Ferguson, R. I., & Parsons, D. R. (2005). A framework for model verification and validation of CFD schemes in natural open channel flows. In P. D. Bates, S. N. Lane, & R. I. Ferguson (Eds.), *Computational fluid dynamics: Applications in environmental hydraulics* (pp. 169–192). Chichester, UK: Wiley. https://doi.org/10.1002/0470015195.ch8

Lane, S. N., & Richards, K. S. (1998). High resolution, two-dimensional spatial modelling of flow processes in a multi-thread channel. *Hydrological Processes*, *12*(8), 1279–1298. https://doi.org/10.1002/(SICI)1099-1085(19980630)12:8<1279::AID-HYP615>3.0.CO;2-E

Lane, S. N., Widdison, P. E., Thomas, R. E., Ashworth, P. J., Best, J. L., Lunt, I. A., et al. (2010). Quantification of braided river channel change using archival digital image analysis. *Earth Surface Processes and Landforms*, *35*, 971–985. https://doi.org/10.1002/esp.2015

Langendoen, E. J., Mendoza, A., Abad, J. D., Tassi, P., Wang, D., Ata, R., et al. (2016). Improved numerical modeling of morphodynamics of rivers with steep banks. *Advances in Water Resources*, *93*, 4–14. https://doi.org/10.1016/j.advwatres.2015.04.002

Lefebvre, A. (2019). Three-dimensional flow above river bedforms: Insights from numerical modeling of a natural dune field (Río Paraná, Argentina). *Journal of Geophysical Research: Earth Surface*, *124*, 2241–2264. https://doi.org/10.1029/2018jf004928

Lefebvre, A., Paarlberg, A. J., & Winter, C. (2016). Characterising natural bedform morphology and its influence on flow. *Geo-Marine Letters*, *36*(5), 379–393. https://doi.org/10.1007/s00367-016-0455-5

Lefebvre, A., & Winter, C. (2016). Predicting bed form roughness: The influence of leeside angle. *Geo-Marine Letters*, *36*(2), 121–133. https://doi.org/10.1007/s00367-016-0436-8

Lunt, I. A., Sambrook Smith, G. H., Best, J. L., Ashworth, P. J., Lane, S. N., & Simpson, C. J. (2013). Deposits of the sandy braided South Saskatchewan River: Implications for the use of modern analogs in reconstructing channel dimensions in reservoir characterization. *AAPG Bulletin*, *97*(4), 553–576. https://doi.org/10.1306/09251211152

Maddux, T. B., McLean, S. R., & Nelson, J. M. (2003). Turbulent flow over three-dimensional dunes: 2. Fluid and bed stresses. *Journal of Geophysical Research*, *108*(F1), 6010. https://doi.org/10.1029/2003JF000018

Maddux, T. B., Nelson, J. M., & McLean, S. R. (2003). Turbulent flow over three-dimensional dunes: 1. Free surface and flow response. *Journal of Geophysical Research*, *108*(F1), 6009. https://doi.org/10.1029/2003JF000017

Marjoribanks, T. I., Hardy, R. J., Lane, S. N., & Tancock, M. J. (2017). Patch-scale representation of vegetation within hydraulic models. *Earth Surface Processes and Landforms*, *42*(5), 699–710. https://doi.org/10.1002/esp.4015

Mosselman, E., & Binh Le, T. (2016). Five common mistakes in fluvial morphodynamic modeling. *Advances in Water Resources*, *93*, 15–20. https://doi.org/10.1016/j.advwatres.2015.07.025

Mueller, D. S., & Wagner, C. R. (2009). *Measuring discharge with acoustic Doppler current profilers from a moving boat*. Washington D.C: U.S. Geological Survey Techniques and Methods. https://pubs.usgs.gov/tm/3a22/pdf/tm3a22_lowres.pdf

Muste, M., Yu, K., & Spasojevic, M. (2004). Practical aspects of ADCP data use for quantification of mean river flow characteristics; Part I: Moving-vessel measurements. *Flow Measurement and Instrumentation*, *15*(1), 1–16. https://doi.org/10.1016/j.flowmeasinst.2003.09.001

Nabi, M., Kimura, I., Hsu, S. M., Giri, S., & Shimizu, Y. (2015). Computational modeling of dissipation and regeneration of fluvial sand dunes under variable discharges. *Journal of Geophysical Research: Earth Surface*, *120*, 1390–1403. https://doi.org/10.1002/2014JF003364

Nabi, M., Vriend, H. J., Mosselman, E., Sloff, C. J., & Shimizu, Y. (2013). Detailed simulation of morphodynamics: 3. Ripples and dunes. *Water Resources Research*, *49*, 5930–5943. https://doi.org/10.1002/wrcr.20457

Naqshband, S., Ribberink, J. S., Hurther, D., & Hulscher, S. J. M. H. (2014). Bed load and suspended load contributions to migrating sand dunes in equilibrium. *Journal of Geophysical Research: Earth Surface*, *119*, 1043–1063. https://doi.org/10.1002/2013JF003043

Nelson, J. M. (1990). The initial instability and finite-amplitude stability of alternate bars in straight channels. *Earth Science Reviews*, *29*(1–4), 97–115. https://doi.org/10.1016/0012-8252(0)90030-Y

Nicholas, A. P. (2013). Modeling the continuum of river channel patterns. *Earth Surface Processes and Landforms*, *38*(10), 1187–1196. https://doi.org/10.1002/esp.3431

Nicholas, A. P., Ashworth, P. J., Sambrook Smith, G. H., & Sandbach, S. D. (2013). Numerical simulation of bar and island morphodynamics in anabranching megarivers. *Journal of Geophysical Research: Earth Surface*, *118*, 2019–2044. https://doi.org/10.1002/jgrf.20132

Nield, J. M., Wiggs, G. F. S., Baddock, M. C., & Hipondoka, M. H. T. (2017). Coupling leeside grainfall to avalanche characteristics in aeolian dune dynamics. *Geology*, *45*(3), 271–274. https://doi.org/10.1130/G38800.1

Omidyeganeh, M. H., & Piomelli, U. (2013a). Large-eddy simulation of three-dimensional dunes in a steady, unidirectional flow. Part 1. Turbulence statistics. *Journal of Fluid Mechanics*, *721*, 454–483. https://doi.org/10.1017/jfm.2013.36

Omidyeganeh, M. H., & Piomelli, U. (2013b). Large-eddy simulation of three-dimensional dunes in a steady, unidirectional flow. Part 2. Flow structures. *Journal of Fluid Mechanics*, *734*, 509–534. https://doi.org/10.1017/jfm.2013.499

Osada, K., Ettema, R., Shimizu, Y., & Wakai, A. (2020). Influence of channel morphology on ice conveyance and bridging: Experiments with a numerical model. *Journal of Cold Regions Engineering*, *34*(1), 04019017. https://doi.org/10.1061/(ASCE)CR.1943-5495.0000201

Parker, N. O., Sambrook Smith, G. H., Ashworth, P. J., Best, J. L., Lane, S. N., Lunt, I. A., et al. (2013). Quantification of the relation between surface morphodynamics and subsurface sedimentological product in sandy braided rivers. *Sedimentology*, *60*(3), 820–839. https://doi.org/10.1111/j.1365-3091.2012.01364.x

Parsons, D. R., Best, J. L., Lane, S. N., Orfeo, O., Hardy, R. J., & Kostaschuk, R. (2007). Form roughness and the absence of secondary flow in a large confluence—Diffluence, Rio Paraná, Argentina. *Earth Surface Processes and Landforms*, *162*, 155–162. https://doi.org/10.1002/esp

Parsons, D. R., Best, J. L., Orfeo, O., Hardy, R. J., Kostaschuk, R., & Lane, S. N. (2005). Morphology and flow fields of three-dimensional dunes, Rio Parana Argentina: Results from simultaneous multibeam echo sounding and acoustic Doppler current profiling. *Journal of Geophysical Research*, *110*, F04S03. https://doi.org/10.1029/2004JF000231

Parsons, D. R., Jackson, P. R., Czuba, J. A., Engel, F. L., Rhoads, B. L., & Oberg, K. A. (2013). Velocity Mapping Toolbox (VMT): A processing and visualization suite for moving-vessel ADCP measurements. *Earth Surface Processes and Landforms*, *38*(11), 1244–1260. https://doi.org/10.1002/esp.3367

Patankar, S. V., & Spalding, D. B. (1972). A calculation procedure for heat, mass and momentum transport in three-dimensional parabolic flows. *International Journal of Heat and Mass Transfer*, *15*(10), 1787–1806. https://doi.org/10.1016/0017-9310(72)90054-3

Pelletier, J. D., Sherman, D. J., Ellis, J. T., Farrell, E. J., Jackson, N. L., Li, B., et al. (2015). Dynamics of sediment storage and release on aeolian dune slip faces: A field study in Jericoacoara, Brazil. *Journal of Geophysical Research: Earth Surface*, *120*, 1911–1934. https://doi.org/10.1002/2015JF003636

Robertson, E., Choudhury, V., Bhushan, S., & Walters, D. K. (2015). Validation of OpenFOAM numerical methods and turbulence models for incompressible bluff body flows. *Computers and Fluids*, *123*, 122–145. https://doi.org/10.1016/j.compfluid.2015.09.010

Rodrigues, S., Mosselman, E., Claude, N., Wintenberger, C. L., & Juge, P. (2015). Alternate bars in a sandy gravel bed river: Generation, migration and interactions with superimposed dunes. *Earth Surface Processes and Landforms*, *40*(5), 610–628. https://doi.org/10.1002/esp.3657

Rubin, D. M. (2012). A unifying model for planform straightness of ripples and dunes in air and water. *Earth-Science Reviews*, *113*(3–4), 176–185. https://doi.org/10.1016/j.earscirev.2012.03.010

Sambrook Smith, G. H., Ashworth, P. J., Best, J. L., Woodward, J., & Simpson, C. J. (2006). The sedimentology and alluvial architecture of the sandy braided South Saskatchewan River, Canada. *Sedimentology*, *53*(2), 413–434. https://doi.org/10.1111/j.1365-3091.2005.00769.x

Sambrook Smith, G. H., Best, J. L., Ashworth, P. J., Lane, S. N., Parker, N. O., Lunt, I. A., et al. (2010). Can we distinguish flood frequency and magnitude in the sedimentological record of rivers? *Geology*, *38*(7), 579–582. https://doi.org/10.1130/g30861.1

Sandbach, S. D., Lane, S. N., Hardy, R. J., Amsler, M. L., Ashworth, P. J., Best, J. L., et al. (2012). Application of a roughness-length representation to parameterize energy loss in 3-D numerical simulations of large rivers. *Water Resources Research*, *48*, W12501. https://doi.org/10.1029/2011WR011284

Sandbach, S. D., Nicholas, A. P., Ashworth, P. J., Best, J. L., Keevil, C. E., Parsons, D. R., et al. (2018). Hydrodynamic modeling of tidal-fluvial flows in a large river estuary. *Estuarine, Coastal and Shelf Science*, *212*(November 2017), 176–188. https://doi.org/10.1016/J.ECSS.2018.06.023

Schmeeckle, M. W. (2014). The role of velocity, pressure, and bed stress fluctuations in bed load transport over bed forms: Numerical simulation downstream of a backward-facing step. *Earth Surface Dynamics*, *3*, 105–112. https://doi.org/10.5194/esurf-3-105-2015

Schuurman, F., & Kleinhans, M. G. (2015). Bar dynamics and bifurcation evolution in a modeled braided sand-bed river. *Earth Surface Processes and Landforms*, *40*(10), 1318–1333. https://doi.org/10.1002/esp.3722

Schuurman, F., Kleinhans, M. G., & Middelkoop, H. (2016). Network response to disturbances in large sand-bed braided rivers. *Earth Surface Dynamics*, *4*(1), 25–45. https://doi.org/10.5194/esurf-4-25-2016

Schuurman, F., Marra, W. A., & Kleinhans, M. G. (2013). Physics-based modeling of large braided sand-bed rivers: Bar pattern formation, dynamics and sensitivity. *Journal of Geophysical Research: Earth Surface*, *118*, 2509–2527. https://doi.org/10.1002/2013JF002896

Sekine, M., & Parker, G. (1992). Bed-load transport on transverse slope. I. *Journal of Hydraulic Engineering*, *118*(4), 513–535. https://doi.org/10.1061/(ASCE)0733-9429(1992)118:4(513)

Sieben, J., & Talmon, A. M. (2011). Bed-load transport in obliquely dune-covered riverbeds. *Journal of Hydraulic Research*, *49*(3), 317–324. https://doi.org/10.1080/00221686.2011.566252

Sloff, K., & Mosselman, E. (2012). Bifurcation modeling in a meandering gravel-sand bed river. *Earth Surface Processes and Landforms*, *37*(14), 1556–1566. https://doi.org/10.1002/esp.3305

Stoesser, T., Braun, C., García-Villalba, M., & Rodi, W. (2008). Turbulence structures in flow over two-dimensional dunes. *Journal of Hydraulic*, *134*(1). https://doi.org/10.1061/(ASCE)0733-9429(2008)134:1(42)

Strick, R. J. P., Ashworth, P. J., Sambrook Smith, G. H., Nicholas, A. P., Best, J. L., Lane, S. N., et al. (2019). Quantification of bedform dynamics and bedload sediment flux in sandy braided rivers from airborne and satellite imagery. *Earth Surface Processes and Landforms*, *44*(4), 953–972. https://doi.org/10.1002/esp.4558

Struiksma, N., Olesen, K., Flokstra, C., & Vriend, H. D. (1985). Bed deformation in curved alluvial channels. *Journal of Hydraulic Research*, *23*(1), 57–79. https://doi.org/10.1080/00221688509499377

Sun, J., Lin, B., & Yang, H. (2015). Development and application of a braided river model with non-uniform sediment transport. *Advances in Water Resources*, *81*, 62–74. https://doi.org/10.1016/j.advwatres.2014.12.012

Sutton, S. L. F., McKenna Neuman, C., & Nickling, W. (2013). Lee slope sediment processes leading to avalanche initiation on an aeolian dune. *Journal of Geophysical Research: Earth Surface*, *118*, 1754–1766. https://doi.org/10.1002/jgrf.20131

Szupiany, R. N., Amsler, M. L., Best, J. L., & Parsons, D. R. (2007). Comparison of fixed and moving vessel measurements with an aDp in a large river. *Journal of Hydraulic Engineering*, *133*(12), 1299–1309. https://doi.org/10.1061/(ASCE)0733-9429(2007)133:12(1299)

Szupiany, R. N., Amsler, M. L., Hernandez, J., Parsons, D. R., Best, J. L., Fornari, E., & Trento, A. (2012). Flow fields, bed shear stresses, and suspended bed sediment dynamics in bifurcations of a large river. *Water Resources Research*, *48*, W11515. https://doi.org/10.1029/2011WR011677

Talmon, A. M., Struiksma, N., & Van Mierlo, M. C. L. M. (1995). Laboratory measurements of the direction of sediment transport on transverse alluvial-bed slopes. *Journal of Hydraulic Research*, *33*(4), 495–517. https://doi.org/10.1080/00221689509498657

Talmon, A. M., Wiesemann, J. (2006). Influence of grain size on the direction of bed load transport on transverse sloping beds, *Proceedings Third International Conference on Scour and Erosion* (pp. 632–639). https://repository.tudelft.nl/islandora/object/uuid%3A0ff8ac8b-3942-43b7-be76-5e7b7a95455

Terwisscha van Scheltinga, R. C., Coco, G., Kleinhans, M. G., & Friedrich, H. (2020). Observations of dune interactions from DEMs using through-water structure from motion. *Geomorphology*, *359*, 107126. https://doi.org/10.1016/j.geomorph.2020.107126

Unsworth, C. A., Nicholas, A. P., Ashworth, P. J., Simpson, C. J., Best, J. L., Lane, S. N., & Sambrook-Smith, G. H. (2016). Using bedform migration and orientation to infer sediment transport pathways in a sandy braided river. In G. S. Constantinescu, M. Garcia, & D. M. Hanes (Eds.), *River Flow 2016: Iowa City, USA, July 11-14, 2016* (pp. 1138–1143). London, UK: Taylor & Francis.

Walker, I. J. (1999). Secondary airflow and sediment transport in the lee of a reversing dune. *Earth Surface Processes and Landforms*, *24*(5), 437–448. https://doi.org/10.1002/(SICI)1096-9837(199905)24:5<437::AID-ESP999>3.0.CO;2-Z

Walker, I. J., & Shugar, D. H. (2013). Secondary flow deflection in the lee of transverse dunes with implications for dune morphodynamics and migration. *Earth Surface Processes and Landforms*, *38*(14), 1642–1654. https://doi.org/10.1002/esp.3398

Weij, B. D. (2012). The interaction between bed-load transport and dune orientation. Masters Thesis, Deflt, Netherlands.

Weller, H. G., Tabor, G., Jasak, H., Fureby, C., & Jasak, H. (1998). A tensorial approach to computational continuum mechanics using object-oriented techniques. *Computational Physics*, *12*(6), 620–631. https://doi.org/10.1063/1.168744

Wiebe, K. L., & Drennan, L. (1973). Sedimentation in reservoirs. In *Fluvial processes and sedimentation, proceedings of Hydrology Symposium, May 8–9, 1973, Edmonton* (pp. 538–579). Ottawa: National Research Council.

Wren, D. G., Kuhnle, R. A., & Wilson, C. G. (2007). Measurements of the relationship between turbulence and sediment in suspension over mobile sand dunes in a laboratory flume. *Journal of Geophysical Research*, *112*, F03009. https://doi.org/10.1029/2006JF000683

Wu, W., Rodi, W., & Wenka, T. (2000). 3-D numerical modeling of water flow and sediment transport in open channels. *Journal of Hydraulic Engineering ASCE*, *126*(1), 4–15.

Xie, Z., Lin, B., Falconer, R. A., & Maddux, T. B. (2013). Large-eddy simulation of turbulent open-channel flow over three-dimensional dunes. *Journal of Hydraulic Research*, *51*(5), 494–505. https://doi.org/10.1080/00221686.2013.835287

Yakhot, V., & Orszag, S. A. (1986). Renormalization group analysis of turbulence. I. Basic theory. *Journal of Scientific Computing*, *1*(1), 3–51. https://doi.org/10.1007/BF01061452

Yamaguchi, S., Giri, S., Shimizu, Y., & Nelson, J. M. (2019). Morphological computation of dune evolution with equilibrium and non-equilibrium sediment-transport models. *Water Resources Research*, *55*, 8463–8477. https://doi.org/10.1029/2018WR024166

Zgheib, N., & Balachandar, S. (2019). On the role of sidewalls in the transition from straight to sinuous bedforms. *Geophysical Research Letters*, *46*, 9612–9619. https://doi.org/10.1029/2019GL084098